

VALIDATION OF STRESSES CAUSED BY THERMAL GRADIENTS IN SEGMENTAL  
CONCRETE BRIDGES – PHASE II

By

NATHAN CURRIER

A THESIS PRESENTED TO THE GRADUATE SCHOOL  
OF THE UNIVERSITY OF FLORIDA IN PARTIAL FULFILLMENT  
OF THE REQUIREMENTS FOR THE DEGREE OF  
MASTER OF ENGINEERING

UNIVERSITY OF FLORIDA

2009

© 2009 Nathan Currier

To Dad and Mom

## ACKNOWLEDGMENTS

I would like to thank Dr. H.R. Hamilton and Dr. G.R. Consolazio for their help and guidance throughout the course of my study at the University of Florida. I would like to thank Dr. R. Cook for sitting on my committee and for the insightful suggestions. I would like to acknowledge and thank the Florida Department of Transportation for funding this research. I would like to further acknowledge and thank DYWIDAG Systems Incorporated (DSI) and W.R. Grace Construction Products for their donations and contribution to this research. Finally, I would like to express my sincere gratitude to Mr. Charles “Chuck” Broward of the University of Florida Structures Laboratory, his staff of undergraduate students, and Mr. Hubert “Nard” Martin for their various contributions towards the successful execution of experiments in the laboratory.

## TABLE OF CONTENTS

	<u>page</u>
ACKNOWLEDGMENTS.....	4
LIST OF TABLES.....	7
LIST OF FIGURES.....	8
ABSTRACT .....	11
CHAPTER	
1 INTRODUCTION .....	13
2 SCOPE AND OBJECTIVES .....	15
3 BACKGROUND .....	16
Thermal Gradient.....	16
Structural Response / Self-Equilibrating Stress .....	17
Phase I Research .....	21
Cracking Behavior .....	23
4 TEST DESIGN.....	32
Approach .....	32
Specimen Design.....	36
Load Frame .....	37
Application of Thermal Gradient .....	38
Concrete Mixture Design .....	39
5 INSTRUMENTATION .....	48
Electrical Resistance Concrete Strain Gauges .....	48
Thermocouples .....	49
Load Cells.....	49
Linear Variable Displacement Transducers .....	49
Data Acquisition System .....	50
Acoustic Emissions.....	50
Background Information and Motivation .....	50
Introduction.....	51
Structural Assessment Techniques .....	52
Acoustic Emission Instrumentation.....	52
6 TEST PROCEDURE.....	58

	Prestressing .....	58
	Concrete Placement .....	59
	Non-Thermal Test .....	60
	Thermal Test .....	60
7	RESULTS AND DISCUSSION .....	63
	Strain – Load Analysis .....	67
	Behavior .....	69
	Analysis .....	73
	Cracking Behavior .....	75
8	SUMMARY AND CONCLUSIONS .....	86
9	RECOMMENDATIONS .....	88
APPENDIX		
A	TEST RESULT FIGURES .....	89
B	TEST RESULT TABLES .....	96
C	LOAD FRAME SHOP DRAWINGS .....	98
D	SPECIMEN DESIGN AND TEST SETUP DRAWINGS .....	105
	LIST OF REFERENCES .....	107
	BIOGRAPHICAL SKETCH .....	109

## LIST OF TABLES

<u>Table</u>		<u>page</u>
3-1	Positive thermal gradient magnitudes.....	27
4-1	Concrete mix design properties.....	40
4-2	Concrete mix design proportions.....	40
4-3	Concrete mixture compressive strength and modulus of rupture.....	40
6-1	Sequence of stages for prestressed non-thermal specimen.....	61
6-2	Sequence of stages for prestressed thermal specimen.....	61
B-1	Net tensile load at initial microcracking for non-thermal and thermal tests .....	96
B-2	Net tensile load at visible cracking for non-thermal and thermal tests .....	96
B-3	Initial stress ratio for non-thermal and thermal tests .....	96
B-4	Final stress ratio for non-thermal and thermal tests.....	97

## LIST OF FIGURES

<u>Figure</u>	<u>page</u>
3-1 Conditions for the development of positive thermal gradients .....	27
3-2 Conditions for the development of negative thermal gradients .....	28
3-3 Positive vertical temperature gradient for concrete superstructures .....	28
3-4 Solar radiation zones for the United States .....	29
3-5 Development of self-equilibrating thermal stresses for positive thermal gradient .....	29
3-6 Development of self-equilibrating thermal stresses for negative thermal gradient .....	30
3-7 Post tensioned T beam segments with test setup in laboratory .....	30
3-8 I-section representation of SRB Bridge cross section.....	31
4-1 Typical cross section of Santa Rosa Bay Bridge .....	40
4-2 SRB Bridge stress profiles.....	41
4-3 Stress profiles of SRB Bridge over the web, SRB Bridge away from the web, and test specimen. ....	42
4-4 Load frame used to test concrete specimens .....	43
4-5 Prestressed concrete specimen schematic .....	43
4-6 Prestressed specimen design.....	44
4-7 Prestressed specimen design.....	45
4-8 Acrylic plate installed in specimen .....	45
4-9 Load frame with specimen and instrumentation .....	45
4-10 Test setup for prestress specimen.....	46
4-11 Top view of prestress locking seat with locking nut and washer setup and side view section of beveled washer and locking nut .....	46
4-12 Load frame with thermal application setup .....	46
4-13 Load frame with open-channel on thermal test specimen .....	47

5-1	Instrumentation setup .....	53
5-2	Strain gauge location and nomenclature for the prestressed thermal specimen and prestressed non-thermal specimen .....	54
5-3	Strain gauge placement on right face of prestressed thermal specimen .....	54
5-4	Prestressed thermal specimen assembled in formwork .....	55
5-5	Thermocouple locations and nomenclature for prestressed thermal specimen ..	55
5-6	Applied load measure by load cell and applied by hydraulic jack .....	56
5-7	Waveform generated by a sensor “hit” .....	56
5-8	DISP-16 Channel Acoustic Emission System.....	57
5-9	R31-AST Piezoelectric Sensor .....	57
5-10	Acoustic Emissions sensor placement and nomenclature .....	57
6-1	Load frame assembly prior to concrete placement.....	62
6-2	Stress state of each stage: prestress, direct tensile loading, self-equilibrating thermal stress, and combined thermal and direct tensile loading .....	62
7-1	Test A – measured thermal gradient and calculated self-equilibrating strain gradient .....	78
7-2	Test A and SRB comparison of thermal gradients and self-equilibrating strain gradients.....	79
7-3	Test A measured strain components from thermal specimen and non-thermal specimen .....	79
7-4	Test A - Non-thermal specimen .....	80
7-5	Test A - Thermal specimen .....	80
7-6	Test A Load-Displacement of Thermal specimen.....	81
7-7	Test A - Crack on right face and left face of thermal test specimen.....	81
7-8	Axial stiffness of specimen and system .....	82
7-9	Idealized test data set and terminology .....	83
7-10	Test A - thermal specimen (stress ratio).....	84

7-11	Test A non-thermal specimen (stress ratio).....	85
7-12	Stress ratio ranges of microcracking .....	85
A-1	Test A results for non-thermal specimen and thermal specimen .....	90
A-2	Test B results for non-thermal specimen and thermal specimen .....	91
A-3	Test C results for non-thermal specimen and thermal specimen.....	92
A-4	Test D results for non-thermal specimen and thermal specimen.....	93
A-5	Test E results for non-thermal specimen and thermal specimen .....	94
A-6	Test F results for non-thermal specimen and thermal specimen .....	95
C-1	Frame overview .....	99
C-2	End frame detail .....	100
C-3	Column detail.....	101
C-4	Plate detail 1 .....	102
C-5	Plate detail 2.....	103
C-6	Prestress chair detail .....	104
D-1	Specimen fabrication drawings.....	105
D-2	Test setup detail .....	106

Abstract of Thesis Presented to the Graduate School  
of the University of Florida in Partial Fulfillment of the  
Requirements for the Degree of Master of Engineering

VALIDATION OF STRESSES CAUSED BY THERMAL GRADIENTS IN SEGMENTAL  
CONCRETE BRIDGES – PHASE II

By

Nathan Currier

December 2009

Chair: H.R. Hamilton  
Cochair: Gary R. Consolazio  
Major: Civil Engineering

Nonlinear thermal gradients have been measured on concrete bridges in the field and previous research, Phase I of this investigation, confirmed that the self-equilibrating stresses generated by the nonlinear portion of such gradients compare well with those calculated by elastic mechanics principles. The research presented in this report evaluated the effect that these self-equilibrating stresses have on the cracking behavior of concrete when superimposed on the stresses due to locked-in and applied moments.

According to *AASHTO Guide Specifications for Design and Construction of Segmental Concrete Bridges* (1999), service stresses resulting from thermal gradients must be superimposed on those caused by dead loads, superimposed service loads, creep, and shrinkage. Thermal gradients considered in bridge design include uniform seasonal temperature variation and nonlinear diurnal temperature variation. Of interest in this investigation is the structural response to the self-equilibrating stress generated by the nonlinear thermal gradient outlined in the *AASHTO Guide Specifications, Thermal Effects in Concrete Bridge Superstructures* (1989).

Prestressed concrete specimens were constructed to replicate the top 8 in. of a segmental concrete bridge deck where the self-equilibrating stresses cause net tension. A series of six test sets were performed during the experimental research. The specimens were initially prestressed and then loaded in tension until a crack formed. The objective was to determine the effect of an applied nonlinear thermal gradient on the cracking stress and behavior of the concrete specimen relative to a specimen that had no thermal gradient applied. A negative nonlinear thermal gradient was applied to one specimen from each test set using an open-channel flow of chilled water. The specimens were each loaded to failure and the results of each test set compared.

The comparison of results from each test set led to no discernable effect of the negative nonlinear thermal gradient on cracking behavior of the concrete. Rather, the influence of variability associated with the cracking behavior of concrete in tension dominated any influence the negative nonlinear thermal gradient may have.

## CHAPTER 1 INTRODUCTION

Nonlinear thermal gradients have been measured on concrete bridges in the field and previous research, Phase I of this investigation (Mahama et al. 2007), confirmed that the self-equilibrating stresses generated by the nonlinear portion of such gradients compare well with those calculated by elastic mechanics principles. The focus of the current phase of research, Phase II, was to determine the effect that these thermal stresses have on the cracking behavior of concrete when superimposed on the stresses due to locked-in and applied moments.

The AASHTO *Guide Specifications for Design and Construction of Segmental Concrete Bridges* (1999) specifies that thermal gradients must be considered in serviceability limit states, along with dead loads, superimposed service loads, creep, and shrinkage. The stresses resulting from thermal gradients are superimposed with the required service load combinations. Thermal gradients considered in bridge design include uniform seasonal temperature variation and nonlinear diurnal temperature variation. Of interest in this investigation is the structural response to the nonlinear thermal gradient outlined in the AASHTO *Guide Specifications, Thermal Effects in Concrete Bridge Superstructures* (1989).

As in Phase I, the Santa Rosa Bay (SRB) Bridge located near Milton, FL was used as a prototype. Ideally, multiple full scale models of the SRB Bridge would be constructed and tested with and without nonlinear thermal gradients concurrently with mechanical load. To avoid the necessity of constructing a full scale specimen to test cracking, a component test specimen representative of the top of the SRB section was designed and tested. Identical specimens were load tested, including the effect of

prestressing, to the point of cracking with and without an applied nonlinear thermal gradient. The results of these tandem tests were compared to determine the effect that the self-equilibrating stresses had on the cracking behavior of the concrete specimen.

Chapter 2 of this report presents the scope and objectives of the investigation. Chapter 3 presents a literature review on the development of thermal gradients, structural response to thermal gradients, a review of Phase I of this project; and cracking behavior in concrete. Chapter 4 describes the development of the test specimen and test design. Chapter 5 provides information on test instrumentation and Chapter 6 outlines the test procedure. Chapter 7 discusses the findings and results from the tests and chapter 8 summarizes the investigation and presents conclusions.

## CHAPTER 2 SCOPE AND OBJECTIVES

Phase I of this research confirmed that the stresses associated with nonlinear thermal gradients do indeed follow those calculated elastically from the thermal gradients and that significant tensile stresses can be developed in the top few inches of the flanges of segmental concrete bridges. Under certain design conditions, when the self-equilibrating thermal stresses are superimposed with stresses caused by mechanical load, significant (and perhaps excessive) prestressing may need to be added to offset the tensile stresses. The added prestressing is needed to avoid or reduce the impact of concrete cracking, which is a serviceability consideration but not a strength consideration. The research presented in this report focuses on evaluating the effect that self-equilibrating thermal stresses have on cracking and the necessity of considering superposition of the full self-equilibrating stresses for serviceability design checks.

## CHAPTER 3 BACKGROUND

### **Thermal Gradient**

Thermal gradients in concrete bridges are caused by the low thermal conductivity of concrete. Diurnal temperature effects from environmental factors such as solar radiation, wind, and ambient air temperatures affect the development of thermal gradients. Concrete material properties such as thermal conductivity, density, and specific heat also factor into the development of thermal gradients (AASHTO 1989). Two gradients develop depending on the environmental conditions. A positive gradient (Figure 3-1) develops when the temperature of the deck is warmer than that of the web. Inversely, a negative gradient (Figure 3-2) develops when the temperature of the deck is cooler than that of the web. Mahama et al. (2007) explains the development of these gradients in greater detail.

Thermal gradients were first introduced into the *AASHTO Guide Specifications, Thermal Effects in Concrete Bridge Superstructures* (1989). Field studies conducted since this publication have led to further development of the thermal gradients used in the design of concrete bridges (Mahama et al. 2007). Thermal gradients published in the *AASHTO Guide Specifications for Design and Construction of Segmental Concrete Bridges* (1999) are currently in use today in design and are used in this research.

The AASHTO (1999) Guide Specifications specify a nonlinear positive thermal gradient as show in Figure 3-3. The vertical dimension “A” is taken as 12 in. for superstructure depths greater than 16 in. and is taken as 4 in. less than the depth of the superstructure if the superstructure depth is less than 16 in. The temperature differentials T1 and T2 are based on the geographic location and the resulting solar

radiation zone. The United States is divided into four solar radiation zones as shown in Figure 3-4. The magnitudes of the temperature differentials for each zone are shown in Table 3-1 (Florida is in zone 3). The bottom temperature differential,  $T_3$ , is specified to be taken as zero unless a value is determined in a site-specific study, but shall be taken to be no greater than 5 °F (AASHTO 1999). Since a site-specific study is generally difficult to obtain, it is typical in design to consider  $T_3$  as zero. The negative thermal gradient is specified in the AASHTO Guide Specifications (1999) using a fractional multiple of the positive gradient (-0.30 for plain concrete surfaces and -0.20 for surfaces with 2-in. asphalt topping).

### **Structural Response / Self-Equilibrating Stress**

Structural response to a nonlinear thermal gradient can be divided into three components: axial expansion, flexural deformation, and internal stress. Axial expansion results from the uniform component of the thermal gradient. Axial forces may develop if the structure is restricted from free thermal expansion. Similarly, flexural deformation occurs as a result of the linear component of the thermal gradient. If the structure is restrained from flexural deformations (e.g. continuous span with restraints from vertical supports) then restraining moments will develop. The third component, internal stress, or what is known as self-equilibrating stress, is the result of inter-fiber compatibility of a section and the nonlinear component of the thermal gradient. As the name implies, these self-equilibrating stresses sum to a resultant axial force and moment both equal to zero.

Mahama et al. (2007) further explains self-equilibrating stresses. Given a section where the fibers are free to deform independently, imposing a nonlinear positive thermal gradient would deform the section fibers as shown in Figure 3-5. The top fibers would

deform with a greater elongation than the middle and bottom fibers. However, the inter-fiber bonds present in a real beam would prevent this deformation. Mahama et al. states: “If the cross section of the beam is able to resist out-of-plane flexural distortion (which is the case for a beam made of a homogeneous isotropic material undergoing uniform bending), the fibers of the beam will undergo a uniform curvature plus elongation.” Stresses then develop in keeping the deformations of the fibers consistent with the resistance of the cross section to out-of-plane flexural distortion. The resulting self-equilibrating stresses are compressive in the top fibers, tensile in the middle, and again compressive in the bottom fibers of the cross section.

Similarly, imposing a nonlinear negative thermal gradient on a section where the fibers are free to deform independently would result in a deformation of the fibers as shown in Figure 3-6. A greater shortening of the top fibers than the middle or bottom fibers would be observed. To maintain a plane section due to inter-fiber bonds of the section, self-equilibrating stresses are developed. For the nonlinear thermal gradient, the resulting self-equilibrating stresses are tensile in the top fibers, compressive in the middle, and again tensile in the bottom fibers of the section.

The AASHTO *Guide Specifications, Thermal Effects in Concrete Bridge Superstructures* (1989) and the AASHTO *LRFD Design Specifications* (2007) outline an approach to analyze the structural response to the thermal gradients. In this approach, the following assumptions are made based on the one-dimensional beam theory:

- The material is homogeneous and exhibits isotropic behavior.
- Material properties are independent of temperature.
- The material has linear stress-strain and temperature-strain relations. Thus, thermal stresses can be considered independently of stresses or strains imposed by other loading conditions, and the principle of superposition holds.

- The Navier-Bernoulli hypothesis that initially plane sections remain plane after bending is valid.
- The temperature varies only with depth, and is constant at all points of equal depth.
- Longitudinal and transverse thermal responses of the bridge superstructure can be considered independently and the results superimposed.

The procedure to determine the self-equilibrating strains due to a nonlinear thermal gradient is completed in several parts. Throughout this method, the sign convention for tensile stress and strain is positive and compressive stress and strain is negative.

The first step assumes a fully restrained member at the ends with a nonlinear thermal gradient applied. The longitudinal stresses resulting from the imposed nonlinear temperature induced strain on a fully restrained member is provided by:

$$\sigma_t(y) = -1 \cdot (E \cdot \alpha \cdot T(y)) \quad 3-1$$

where  $\sigma_t(y)$  is the longitudinal stress at a fiber located a distance  $y$  from the neutral axis of the cross section,  $E$  is the elastic modulus,  $\alpha$  is the coefficient of thermal expansion, and  $T(y)$  is the temperature at a depth  $y$ . The resulting axial force and moment to maintain full restraint are then determined from the stress distribution:

$$P = \int \sigma_t(y) \cdot b(y) \cdot dy \quad 3-2$$

$$M = \int \sigma_t(y) \cdot b(y) \cdot y \cdot dy \quad 3-3$$

where  $P$  is the restraining axial force,  $M$  is the restraining end moment, and  $b(y)$  is the net section width at depth  $y$ . For statically determinate structures, the self-equilibrating stress is obtained by subtracting the stresses due to the restraining axial

force and restraining end moment from the restrained stress distribution obtained in Equation 3-1. The self-equilibrating stress is therefore:

$$\sigma(y) = \sigma_t(y) - \frac{P}{A} - \frac{M \cdot y}{I} \quad 3-4$$

where  $\sigma_t(y)$  is the self-equilibrating stress distribution,  $A$  is the area of the cross-section, and  $I$  is the moment of inertia of the cross section. The corresponding strain distribution and curvature of the member is:

$$\varepsilon(y) = \frac{-1}{E} \cdot \left( \frac{P}{A} + \frac{M \cdot y}{I} \right) \quad 3-5$$

$$\phi = -\frac{M}{E \cdot I} \quad 3-6$$

where  $\varepsilon(y)$  is the strain distribution of the section and  $\phi$  is the curvature of the member. The self-equilibrating strains, associated with the self-equilibrating thermal stresses, are calculated by simply dividing Equation 3-4 by the modulus of elasticity. Substituting Equation 3-1 and Equation 3-5 into Equation 3-4 yields a simplified calculation of the self-equilibrating strains:

$$\varepsilon_{SE}(y) = \varepsilon(y) - \alpha \cdot T(y) \quad 3-7$$

where  $\varepsilon_{SE}(y)$  is the strain distribution corresponding to the self-equilibrating thermal stresses.

Further, if the structure is statically indeterminate, continuity stresses can be determined using structural analysis software. In this procedure, an analysis is conducted in which the negative of the restraining axial force and bending moment are applied as loads to the continuous structure to obtain the resulting stresses. These

stresses are then superimposed on the statically-determinate self-equilibrating thermal stresses to account for continuity effects (Mahama et al. 2007).

### **Phase I Research**

The research encompassing the validation of stresses caused by thermal gradients in segmental concrete bridges was conducted in two phases. The purpose of Phase I of the research was to specifically quantify self-equilibrating thermal stresses caused by the AASHTO nonlinear thermal gradients in segmental concrete bridges. The intent was to validate the self-equilibrating thermal stress values predicted by the *AASHTO Guide Specifications, Thermal Effects in Concrete Bridge Superstructures* (1999) and the *AASHTO LRFD Design Specifications* (2004). These specifications require the consideration of nonlinear thermal gradient load cases when analyzing a segmental bridge for serviceability. Phase I of this research was conducted by Mahama et al. (2007) at the University of Florida and presented in a dissertation titled: "Validation of Stresses Caused by Thermal Gradients in Segmental Concrete Bridges".

In Phase I, to validate the self-equilibrating thermal stresses caused by the AASHTO design nonlinear thermal gradients, a 20 ft-long 3 ft-deep segmental T beam was constructed and tested in the laboratory (Figure 3-7). The Santa Rosa Bay (SRB) Bridge located near Milton, FL was used as a prototype in the design of the laboratory T beam section. The T beam cross section was a representative section of a modified SRB Bridge section (Figure 3-8). The beam consisted of four 5 ft segments externally post-tensioned together with dry joints and four high high-strength steel bars. The AASHTO design nonlinear thermal gradients were imposed by embedding rows of copper tubing into two of the four beam segments and heating them as necessary by passing heated water through the tubes.

The Phase I experimental program consisted of determining the in-situ coefficient of thermal expansion (CTE) of the heated segments; investigating the behavior of the beam under the action of mechanical loads; applying a uniform temperature change on the heated segments to investigate the free expansion behavior of the beam; and imposing the AASHTO design nonlinear thermal gradients in combination with mechanical loads for the purpose of quantifying self-equilibrating thermal stresses due to the thermal gradients. In short, the Phase I research produced the following conclusions:

- The measured stressed-induced concrete strains in the top 0.5 in. of the flanges, where the maximum stresses were expected to occur, were either unable to be quantified or were an average of 47% and 67% less than the calculated stresses for the positive and negative thermal gradients, respectively. This was attributed to differential shrinkage in the top flange fibers and a probable discontinuity in the thermal gradients within the top 0.5 in. of the flanges of the heated segments.
- At elevations below 0.5 in. from the top surface of the segment flanges, measured stress-induced concrete strains caused by the laboratory-imposed nonlinear thermal gradients agreed well with strains calculated using the AASHTO recommended method for the analysis of nonlinear thermal gradients. Maximum measured stress-induced concrete strains were an average of 5% and 20% less than the calculated stresses for the positive and negative thermal gradients, respectively. The difference of 20% less than the AASHTO calculated stresses for the negative thermal gradient could, however, not be attributed to any flaws in the AASHTO method. They were considered to be likely the result of experimental error.
- The percentage difference between maximum measured and maximum calculated negative gradient stresses was higher than that for the positive thermal gradient because the negative thermal gradient was more sensitive to local deviations of temperature from the width-wise average temperatures that were used in calculating the self-equilibrating thermal stresses. The difference in sensitivity was due to the magnitude of the negative thermal gradient being only 30% the magnitude of the positive thermal gradient.
- Based on the effects that differential shrinkage and slight damage to the top flange surfaces had on the magnitude of quantified stresses, it is possible that self-equilibrating thermal stresses in the top section fibers at dry joints in segmental concrete bridges may be smaller in magnitude than stresses calculated using the AASHTO method.

Given these conclusions, one of the future research recommendations made by Mahama et al. (2007) was:

- “The effect on concrete durability of tensile stresses generated by the AASHTO negative thermal gradient in the top few inches of the flanges of segmental concrete bridges needs investigation. Though tensile stresses have been known to cause damage to concrete, this damage has been difficult to quantify. A study into the effect of the relatively severe self-equilibrating stress gradient in the top few inches of concrete (compared to typical bending stresses) on the potential for cracking would lead to a better understanding of the level of damage that gradient-induced tensile stresses may cause.”

In validating the stresses caused by thermal gradients in segmental concrete bridges, it was appropriate to further investigate the effects of those stresses on concrete durability. The intent of Phase II of this research, reported herein, is to investigate and quantify the damage that is associated with tensile stresses arising from application of the AASHTO negative thermal gradient to the top few inches of the flanges of segmental concrete bridges.

### **Cracking Behavior**

The behavior of cracking in concrete has been widely studied in an attempt to understand the physical limitations of concrete in structural applications. Cracking of concrete is known to occur under both compressive and tensile applications. Fractures in concrete are the result of tensile stresses reaching the tensile strength of concrete, whether such stresses are induced by the application of applied compression or tension (Popovics 1998). Cracking behavior of concrete in compression typically leads to crushing or spalling. Tensile cracking generally occurs due to flexure or direct tension under an applied loading condition. Tensile stresses can also occur due to creep, shrinkage, and temperature effects (ACI Committee 209 2008). As the primary focus of

this research was investigating cracking behavior under tensile loads, tensile cracking will be further discussed in this section.

Cracking in concrete occurs as a progression, starting as internal microcracking and coalescing into a visible macrocrack. The body of knowledge used to describe this behavior of progression and how it starts is known as fracture mechanics. The theories of fracture mechanics generally applies to most brittle materials. This area of study is vast including “fundamental theories as well as experimentation and phenomenological work” (Popovics 1998). As such, attempts to develop a sufficient quantitative theory of fracture behavior have only been partially successful for any material. Attempts made in concrete have been even less successful in developing a sufficient quantitative theory of fracture behavior. One reason for this lack of success is that concrete is a highly heterogeneous composite material; made up of aggregates and a softer but still brittle cement paste. It needs to be noted that the fracture behavior of concrete is still not fully understood, either at the microscopic or macroscopic levels. As Popovics states, “the problem is still at the stage of description and classification of observed behavior” (1998).

Progression of cracking strongly influences the ultimate failure strength of concrete. Microcracks are known to exist even prior to any load application at the interface between coarse aggregate and cement paste. Such microcracks may exist due to the mechanical property differences between the aggregate and cement, as well as shrinkage and thermal movement. Microcracks in concrete remain stable as compressive load is applied up to approximately 30 percent or more of the ultimate compressive load. Beyond this load level, microcracks slowly propagate as they

increase in size and number. As load continues to be applied up to about 70 to 90 percent of the ultimate compressive load, the microcracks coalesce to form continuous cracks, or macrocracks (Popovics 1998). In regard to strain, Popovics found from several studies that the maximum tensile strain concrete can resist is on the order of approximately 100 microstrain (1998). Zhen-hai and Xiu-qin (1987) identified several studies where the maximum tensile strain at failure varied from 60 to 800 microstrain in different tests.

Several methods have been developed to quantify and compare concrete resistance to tensile stress cracking. These methods include flexural, direct, and indirect measurements. Flexural strength, or the modulus of rupture, which is a calculated tensile strength, can be determined with a small prismatic beam under third-point loading in accordance with ASTM C78 (ASTM C 78-08). Several methods have been used to measure the direct tensile strength of concrete, although none has been standardized in America due to inherent difficulties of applying a uniaxial tension on a concrete specimen. Although not standardized, investigations using this approach have been successful with careful laboratory testing (Popovics 1998). A standardized indirect method of measurement is the split tensile test, specified in ASTM C496 (ASTM C 496-04) using a cylindrical specimen.

While these methods provide measures by which to compare concretes, there is significant variability between methods and even within tests. Between methods, it has been found that the direct tensile strength measured in concrete is about 75% of the modulus of rupture (Neville 1995). Within a given test method, preexisting flaws cause variability of the results. Regarding the modulus of rupture test, Popovics (1998) noted

that flexural strength obtained in the laboratory can have an expected coefficient of variation of about 5% or more. This increases to a coefficient of variation of 12 to 15% in the field. The variability of results from direct tensile tests in laboratories appeared to be the same as the modulus of rupture test conducted in laboratories. ACI 224R (1992) reported a coefficient of variation for typical results of 6%, 7% and 5% for modulus of rupture test, direct tensile test and split tensile test, respectively. In comparing the direct tensile strength to the modulus of rupture, ACI 224R (1992) reported a ratio range of 0.48 to 0.63 for a concrete compressive strength range of 1000 to 9000 psi, respectively.

Extensive investigations in comparing the modulus of rupture to the concrete compressive strength have been conducted to predict the tensile strength of concrete in design. ACI 318 (ACI Committee 318-05 2005) allows the modulus of rupture to be estimated as:

$$f_r = 7.5\sqrt{f'_c} \quad 3-8$$

where  $f_r$  is the modulus of rupture in psi and  $f'_c$  is the concrete compressive strength in psi for normal weight concrete (2005). Popovics summarized numerous approximations found for the relationship between flexural and compressive strengths, noting that ACI Committee 435 estimated the modulus of rupture to be anywhere between  $5\sqrt{f'_c}$  to  $12\sqrt{f'_c}$  in psi (1998). The summary gave a range of the modulus of rupture to compressive strength ratio of 0.09 to 0.29 (Popovics 1998).

The variability seen in measuring the tensile strength of concrete is the result of the inherent variability of the concrete. The concrete matrix contains flaws such as microcracks, voids, and pores. Extensive investigations into the cracking behavior and

tensile strength of concrete have yielded an improved understanding of the tensile strength of concrete, but there still exists significant variability in the nature of cracking in concrete and prediction of the tensile strength of concrete.

Table 3-1. Positive thermal gradient magnitudes  
Plain Concrete Surface or Asphalt Topping

Zone	T <sub>1</sub> (°F)	T <sub>2</sub> (°F)
1	54	14
2	46	12
3	41	11
4	38	9

\*AASHTO (1999)., “Guide Specifications for Design and Construction of Segmental Concrete Bridges,” 2nd Ed., Washington, D.C., Table 6-1, pg. 10.

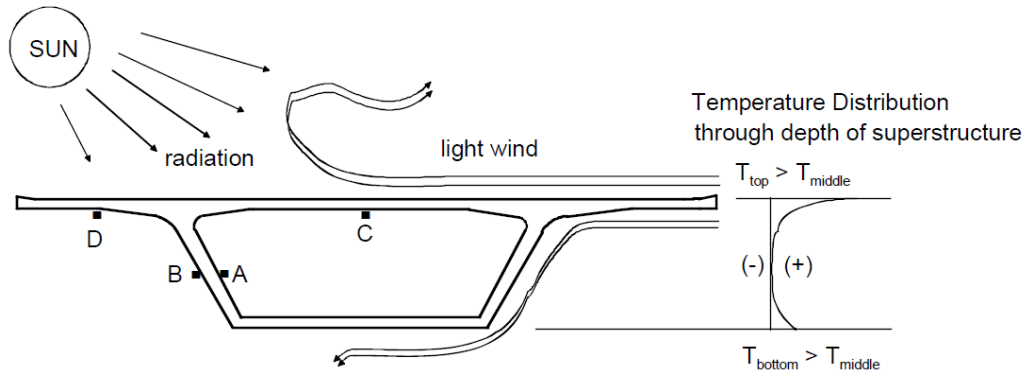


Figure 3-1. Conditions for the development of positive thermal gradients (Mahama et al. (2007)., “Validation of Stresses Caused by Thermal Gradients in Segmental Concrete Bridges,” Figure 3-1, pg. 42)

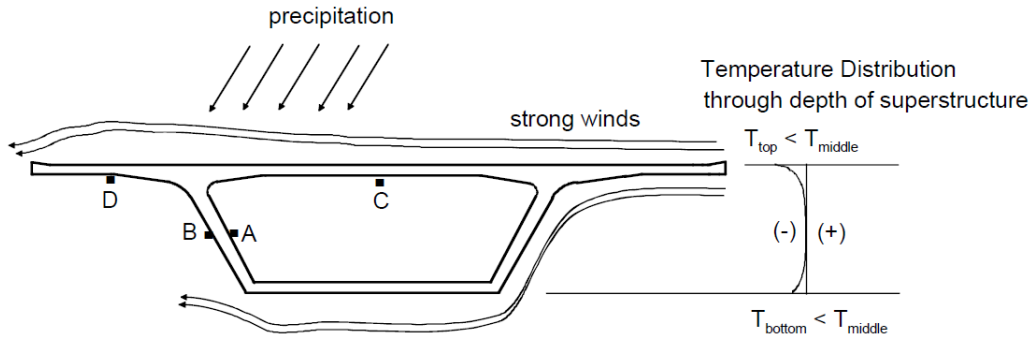


Figure 3-2. Conditions for the development of negative thermal gradients (Mahama et al. (2007)., "Validation of Stresses Caused by Thermal Gradients in Segmental Concrete Bridges," Figure 3-2, pg. 42)

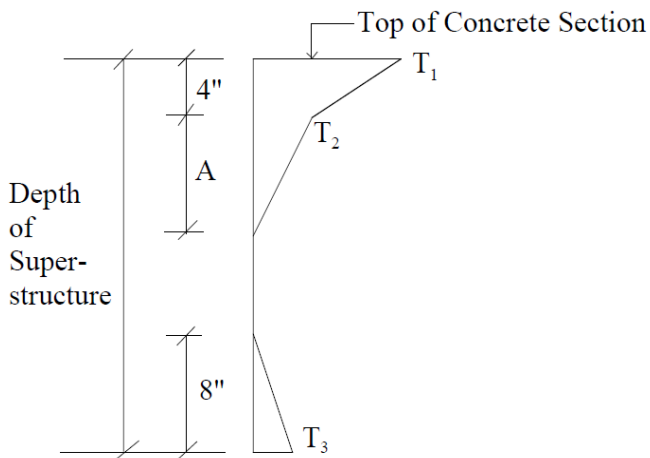


Figure 3-3. Positive vertical temperature gradient for concrete superstructures (AASHTO (1999)., "Guide Specifications for Design and Construction of Segmental Concrete Bridges," 2nd Ed., Washington, D.C., Figure 6-4, pg. 11)

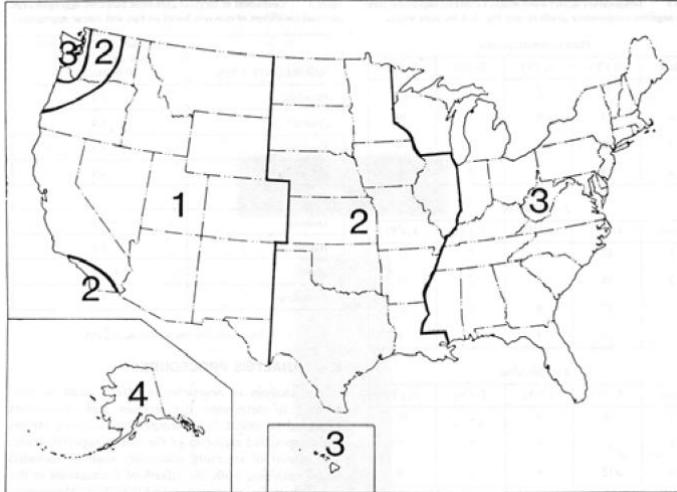


Figure 3-4. Solar radiation zones for the United States (AASHTO (1989a)., "AASHTO Guide Specifications, Thermal Effects in Concrete Bridge Superstructures," Washington D.C., Figure 4, pg. 5)

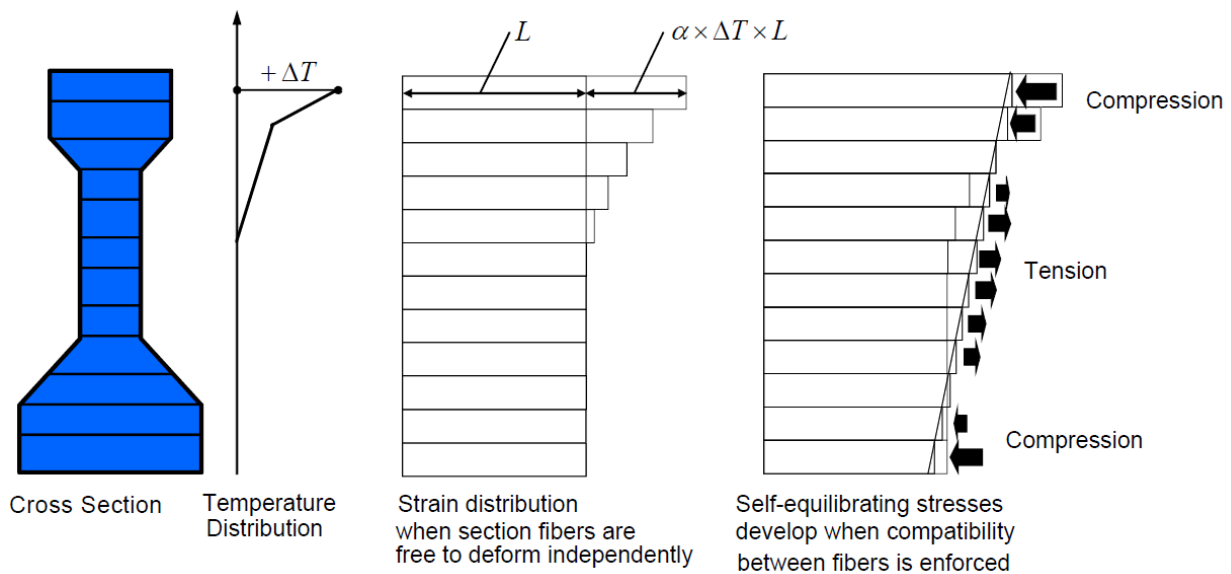


Figure 3-5. Development of self-equilibrating thermal stresses for positive thermal gradient (Mahama et al. (2007)., "Validation of Stresses Caused by Thermal Gradients in Segmental Concrete Bridges," Figure 3-7, pg. 44)

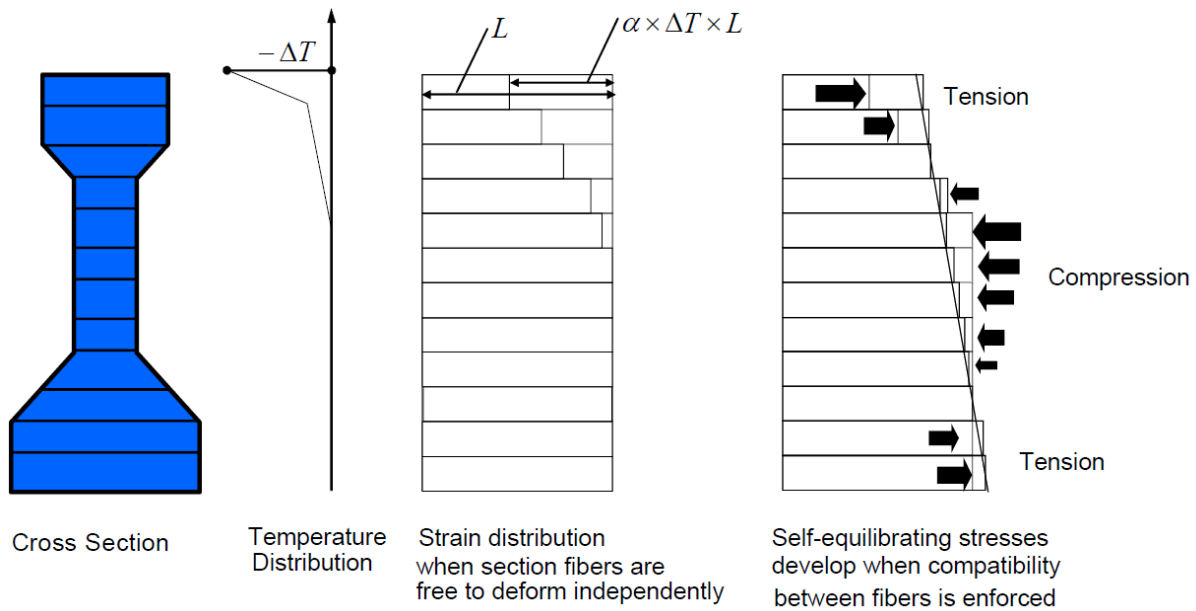


Figure 3-6. Development of self-equilibrating thermal stresses for negative thermal gradient (Mahama et al. (2007)., "Validation of Stresses Caused by Thermal Gradients in Segmental Concrete Bridges," Figure 3-8, pg. 45)

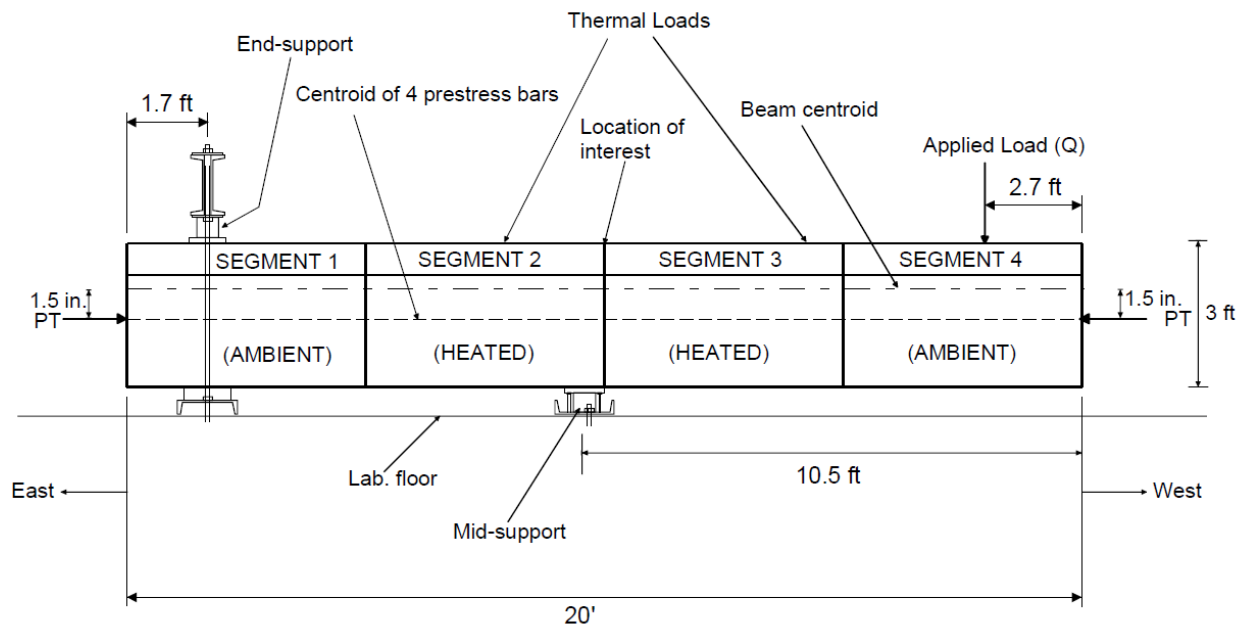


Figure 3-7. Post tensioned T beam segments with test setup in laboratory (Mahama et al. (2007)., "Validation of Stresses Caused by Thermal Gradients in Segmental Concrete Bridges," Figure 7-1, pg. 90)

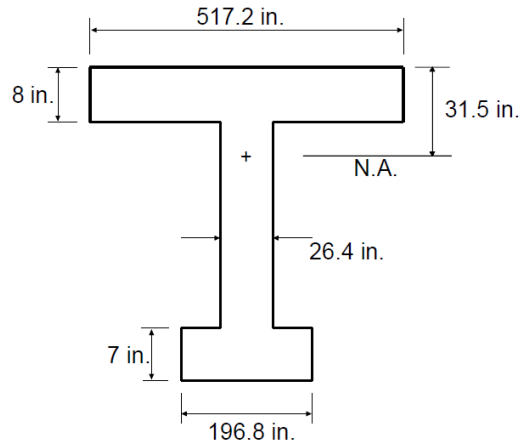


Figure 3-8. I-section representation of SRB Bridge cross section (Mahama et al. (2007)., "Validation of Stresses Caused by Thermal Gradients in Segmental Concrete Bridges," Figure 4-2, pg. 54)

## CHAPTER 4 TEST DESIGN

This section describes the overall test setup, test specimen design, load frame design, setup for thermal application, and concrete mixture design used in the test program. The purpose of the test setup and design of multiple components was to allow for the prestressing and direct tensile loading of the concrete specimens.

### **Approach**

As in Phase I, the Santa Rosa Bay (SRB) Bridge located near Milton, FL was used as a prototype for developing a component specimen that could be used to evaluate the effect of a nonlinear thermal gradient on cracking behavior in concrete. The section immediately adjacent to the pier segment of the SRB Bridge, shown in Figure 4-1, was used to establish the stress states and geometry of the test specimen. The maximum negative moment under combined loads will occur at this location resulting in maximum tensile stresses. The addition of the negative thermal gradient imposes a sharp increase of predicted tensile stress in the top of the SRB Bridge section. This predicted tensile stress resulting from the thermal gradient leads to additional post-tensioning requirements in design.

Initially, the design loads and thermal gradients of the SRB Bridge were investigated over the full height of the box section as shown in the figure. Stress profile components of a simplified load combination for the SRB Bridge are shown in Figure 4-2 for the section immediately adjacent to the pier segment. The stress profiles show the components of prestress, combined dead loads, superimposed service loads, and predicted self-equilibrating stress due to the nonlinear AASHTO negative thermal gradient. The total stress gradient is shown with and without the predicted self-

equilibrating stress. The self-equilibrating stresses create a severe tensile stress gradient in the upper four to six inches of the deck. Although not addressed in the *AASHTO Guide Specifications for Design and Construction of Segmental Concrete Bridges* (1999) it is likely that this stress state is different in the deck away from the web due to shear lag. The deck slab at the tip of the cantilever or midway between the webs does not have the restraint offered by the web for the deck sections over the web. To satisfy the design requirements for serviceability, however, this severe self-equilibrating tensile stress gradient must be offset by prestressing ostensibly over the full width of the slab.

Figure 4-3A shows the stress state in the deck over the web of the SRB Bridge prototype. Each stress block is plotted to scale relative to the zero stress datum and the modulus of rupture ( $f_r$ ). The self equilibrating stresses were calculated with the negative design gradient applied over the full depth of the box section. The service stresses include both the precompression and stresses from applied loads such that the sum of these stresses and the self-equilibrating stresses equal the modulus of rupture. Figure 4-3B shows the stress state of the deck if it were completely unrestrained by the web under the negative design gradient. It has been assumed that the negative thermal gradient developed in the deck away from the web would be that specified by *AASHTO Guide Specifications for Design and Construction of Segmental Concrete Bridges* (1999), shown in Figure 3-3 with the depth “A” taken as 4 in. This gradient produces a minimal self-equilibrating stress profile in the deck away from the web, requiring a higher service stress state to reach the modulus of rupture.

Ideally, multiple full scale models of the SRB Bridge would be constructed and tested with and without nonlinear thermal gradients under an applied mechanical load. This would capture the behavior illustrated in both Figure 4-3A and Figure 4-3B. Laboratory and budget constraints, however, restricted the size of the specimen. Consequently, a portion of the box near the top flange of the box girder (Figure 4-1), where the self-equilibrating stress has a severe gradient relative to that of the imposed stresses, was isolated for use in component testing. These isolated segments were constructed and tested as shown in Figure 4-4 with and without an applied thermal gradient to determine the effect that the gradient has on the cracking behavior of the concrete specimen. Prestressing, tensile loading, application of a nonlinear thermal gradient, constructability, and replication were all considerations in the design and development of the test specimen and procedures. A test specimen section with a depth of 8 in., the thickness of the SRB Bridge deck, was selected. Within this depth in the SRB Bridge deck the stress gradient due to the negative thermal gradient is the most severe and is likely where cracking would occur in the prototype. The stress gradient proposed for the test specimen (Figure 4-3C) was more severe than those likely to result in the prototype either near the web or away from the web. Further, limiting the cross-sectional area allowed a sufficient number of specimens to be economically constructed and tested.

In general, direct or indirect tensile tests of concrete produce lower tensile strengths than the modulus of rupture test that uses flexural tension (Neville 1995). Consequently, more severe tensile strain gradients will tend to cause cracking at higher extreme fiber tensile stresses in specimens with the same concrete. Although the

thermal stress gradient of the SRB Bridge is shallower than that of the specimen, the difference is not considered significant enough to affect the results. Ultimately, the results of tests on identical specimens with and without thermal gradients will be compared to determine if the cracking behavior is affected by the thermal gradients. If the addition of the self-equilibrating stress profile to the uniform direct tensile stress profile causes no significant difference in observed cracking behavior of the concrete specimens, then cracking of the SRB Bridge deck under the addition of the self-equilibrating stress profile would not be expected.

The thermal gradient imposed on the specimen was intended to replicate the natural development (due to environmental conditions) of a thermal gradient and resulting self-equilibrating strain. The target for developing a nonlinear negative thermal gradient on the test specimen was to reach the maximum temperature difference of -12.3 °F at the top surface as specified in the *AASHTO Guide Specifications for Design and Construction of Segmental Concrete Bridges* (1999). The intent was to control the top surface temperature differential in the concrete specimen so that the nonlinear gradient would follow approximately that indicated by AASHTO. Application of the thermal gradient to the test specimen was intended to replicate the severe self-equilibrating tensile strain gradient that is developed in the SRB Bridge with the AASHTO negative thermal gradient.

Prestressing was applied to the concrete specimen to replicate the stress conditions in segmental bridge construction. Specimen prestressing also ensured that cracking did not occur immediately upon application of the thermal gradient. The

uniform compressive prestress applied to the test specimens was the same as that found in the deck of the SRB Bridge.

### **Specimen Design**

Each specimen tested in this study was a 4x8x28 in. prestressed concrete specimen as shown in Figure 4-5. The prestressed specimen was designed to use a central bar and anchors to induce a tensile stress condition and force cracking to occur at the specimen midsection under tensile loading. The specimen was designed such that each half, comprised of an anchor and confinement steel, applied a uniformly distributed stress at the mid-section of the specimen, which was unreinforced and where the stressed bar was debonded.

The specimen design, shown in Figure 4-6, used a steel bar and hardware provided by Dywidag Systems International (DYWIDAG) to apply the prestressing and tensile loading. The steel bar was a 1-in. diameter DYWIDAG threaded bar with an ultimate strength of 150ksi and yield strength of 125ksi. Each anchor was created using two 1-in. diameter hex nuts on either side of a 1.125 in. diameter flat washer. Anchors were placed at the quarter points of the specimen, as measured from the outside face of the washers. The mid-section of the specimen was debonded from the DYWIDAG bar using a 4-in. length of 1-in. diameter PVC pipe. Confinement of the anchors was provided by #3 stirrups, which were tack welded in place as shown in Figure 4-7. The confinement reinforcement was attached to the anchors by a tack weld to the washer within each anchor.

To force cracking to occur at the midsection of the specimen, a 1.25 in. x 0.125 in. acrylic plate was placed vertically above and below the PVC and DYWIDAG bar as shown in Figure 4-8. The plate was sharpened along its edges to encourage crack

initiation at this location. The acrylic plates were constructed from a 1.25 in. wide strip with a 1.25 in. diameter semi-circle cut out of the center, creating two halves with a half circle on each end. These two halves were then affixed to the PVC pipe with glue. Slots cut into each form prevented movement of the ends of the acrylic plates during concrete placement.

### **Load Frame**

The load frame assembly was comprised of a reaction frame, prestressing components, and instrumentation as shown in Figure 4-9 and Figure 4-10. The frame was designed to act as a stand-alone reaction frame and allow the test specimen to first be prestressed and then loaded in tension.

The reaction frame consisted of two short columns placed between built-up reaction beams. Each column was a rectangular tube section with welded end plates, each plate having a center hole for an all-thread bar. Each reaction beam was built-up from two C-channel sections placed back-to-back and spaced with a 1.5 in. gap using plain steel bar. The columns and beams of the reaction frame were held together by two 1 in. diameter all-thread rods placed through the center of the columns.

The specimen was placed in the center of the reaction frame with each end of the DYWIDAG bar extending through the reaction beams. At one end of the DYWIDAG bar, against the outside face of the reaction beam, was placed a load cell between two 1 in. thick DYWIDAG anchor plates and with one DYWIDAG anchor nut placed on the end. At the opposite end of the DYWIDAG bar was placed a prestress locking seat, a hydraulic jack, and an anchor plate and nut on the end. The prestress locking seat was placed with a 1 in. thick plate between itself and the outside face of the reaction beam

as shown in Figure 4-11. The 1 in. plate was used to minimize flexure of the channel flanges and the end plate of the prestress locking seat.

The prestress locking seat, shown in Figure 4-11, was designed to support the hydraulic jack during loading of the DYWIDAG bar and allow for the bar to be locked-off after prestressing. Over-size counter-oriented beveled washers, shown in Figure 4-11B were used to release the locking nut without requiring the application of additional load beyond the prestressing force. A single beveled washer was fixed and the other beveled washer free to slip. The over-size counter-oriented beveled washers allowed for slip in the washers around the DYWIDAG bar. When the free washer was displaced, the vertical slip of the washer reduced the horizontal distance between plates, relieving the locking nut of any load.

### **Application of Thermal Gradient**

To impose a nonlinear thermal gradient on a concrete specimen, an open-channel was constructed as shown in Figure 4-12 and Figure 4-13. The channel was placed on the top surface of the specimen and configured in a closed-loop flow system. The channel was constructed of 0.125 in. thick acrylic sheets with an inflow at one end and a flow spillway at the opposite end. The open channel flow of water was separated from the concrete specimen surface by a thin plastic sheet placed between the specimen and the channel. A silicone adhesive and sealant was used to seal the perimeter of the channel at the plastic sheet. A standard large cooler with a 0.625 in. diameter out flow pipe to a pump and valve was used as a constant-temperature water reservoir.

The nonlinear thermal gradient was imposed using a flow of chilled water over the top of the specimen (Figure 4-12). The water was carried by a closed loop system starting at a reservoir and pumped to the open channel inflow, over the specimen, over

the flow spillway and returning to the reservoir by a shallow return channel. The flow was maintained at a depth of 0.5 in. to 0.75 in. above the surface of the specimen and at a flow of approximately 2.4 gallons per minute. The water in the reservoir was chilled 20°F colder than the initial average temperature of the specimen and maintained using ice. Water flow temperature in the open channel was recorded during testing by the placement of a single thermocouple at 0.25 in. above the top surface.

### **Concrete Mixture Design**

A concrete mixture design was developed to ensure a controlled and consistent mixture throughout testing. The mixture was designed as a high slump and high early strength concrete. Multiple test mixtures were performed prior to testing to ensure consistent concrete properties. The mixture was designed with a water-cement ratio of 0.40 and with a target slump of 9 in. to ensure adequate consolidation in the test specimen forms. A minimum compressive strength of 5000 psi at four days was used to allow for prestressing and testing of the concrete specimens within a single work week, or five day period.

Aggregates, cement, and admixtures were obtained from local vendors and concrete mixing was performed by the author in the Civil Engineering materials lab at the University of Florida, Gainesville, FL. A 3/8 in. maximum diameter coarse aggregate (#89 granite) was obtained from Conrad Yelvington Distributors, Inc., Gainesville, FL. Concrete sand for fine aggregate was obtained from Florida Rock Industries, Inc., Gainesville, FL. The cement used was Type I/II portland cement. Micro-silica fume slurry, Force 10,000 from Grace Construction Products, was used to obtain a high early strength. When required, a high to mid-range water reducer was used to obtain the target slump. The water reducing admixture used was ADVA 140 of Grace Concrete

Products. The mixture design properties are shown in Table 4-1 and the mixture design proportions are shown in Table 4-2. Results for the compressive strength and modulus of rupture tests performed for each test set are shown in Table 4-3.

Table 4-1. Concrete mix design properties

Property	ASTM	
Strength (psi)	C39	7000
W/C Ratio	--	0.40
Slump (in)	C143	9.0 ± 0.5
Plastic Unit Weight (lbs/cf)	C138	143.2 ± 2.0

Table 4-2. Concrete mix design proportions

Material	ASTM	Type	Proportion (lbs/cf)
Cement	C150	I/II	37.7
Cement	C618	Micro-Silica Slurry	0.36
Water	--	--	6.02
Fine Aggregate	C33	Sand	61.6
Aggregate	C33	#89 Granite	37.6
Admixture	C494	Water Reducer	Dosage rates vary

Table 4-3. Concrete mixture compressive strength and modulus of rupture

Compressive Strength (psi)	Test A	Test B	Test C	Test D	Test E	Test F
@ 4 days (testing)	5262	5183	5727	5448	5609	5463
@ 7 days	5863	6060	6044	6032	6398	6247
@ 28 days	6948	7594	7414	7319	7952	7547
Modulus of Rupture (psi)						
@ 4 days (testing)	749	705	767	703	685	650

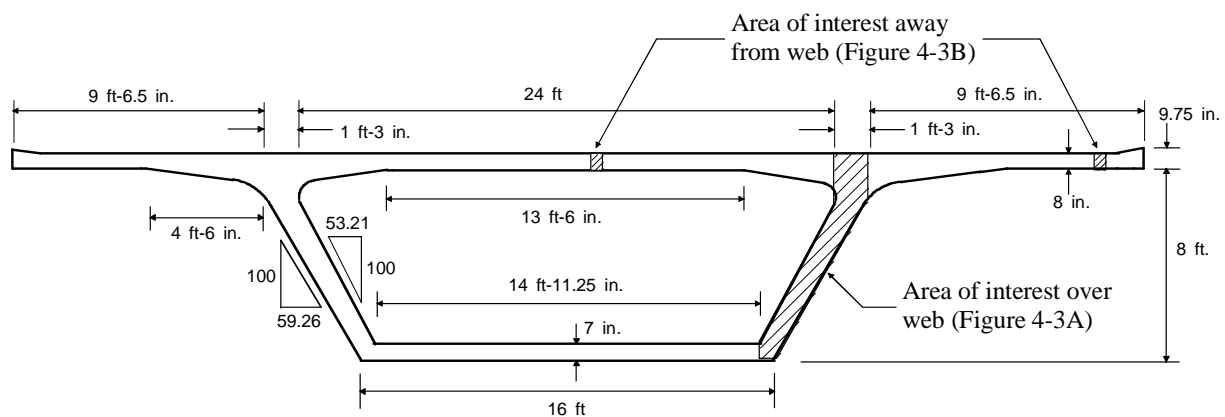


Figure 4-1. Typical cross section of Santa Rosa Bay Bridge

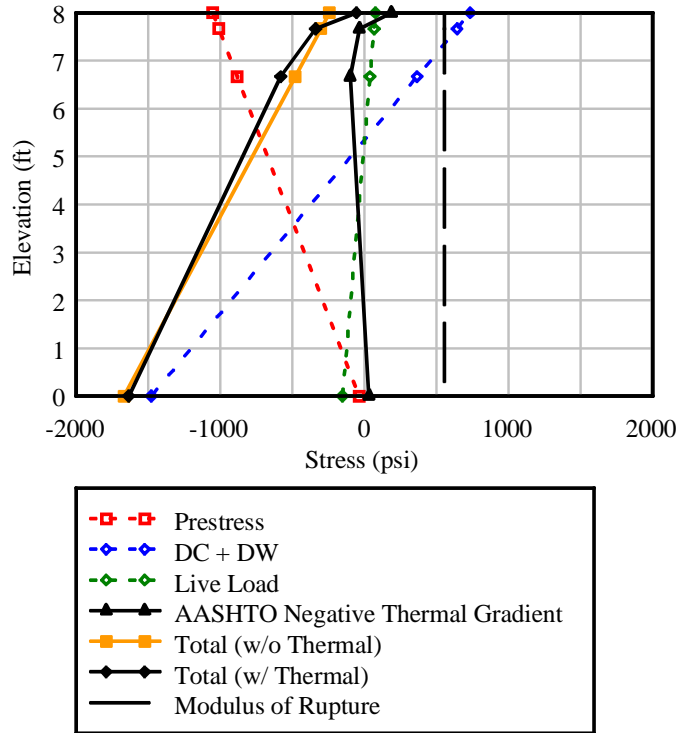


Figure 4-2. SRB Bridge stress profiles

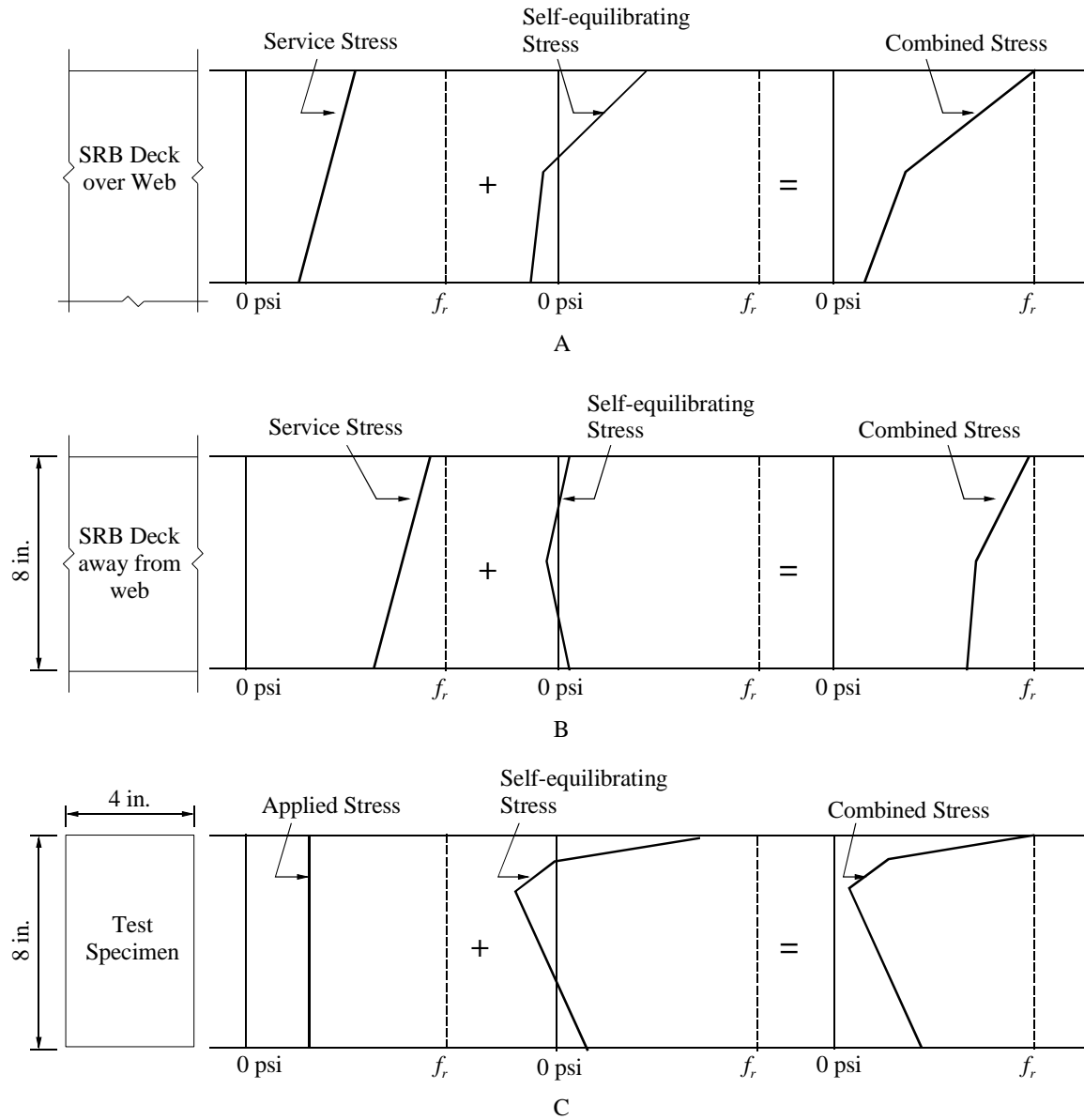


Figure 4-3. Stress profiles of A) SRB Bridge over the web, B) SRB Bridge away from the web, and C) test specimen.

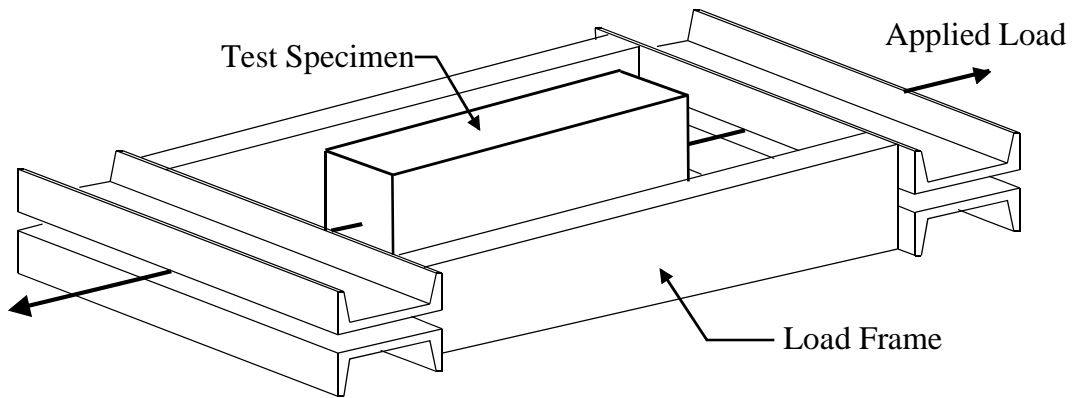


Figure 4-4. Load frame used to test concrete specimens

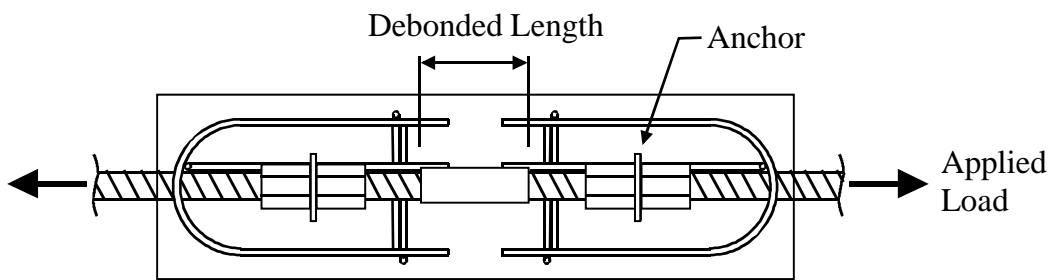


Figure 4-5. Prestressed concrete specimen schematic



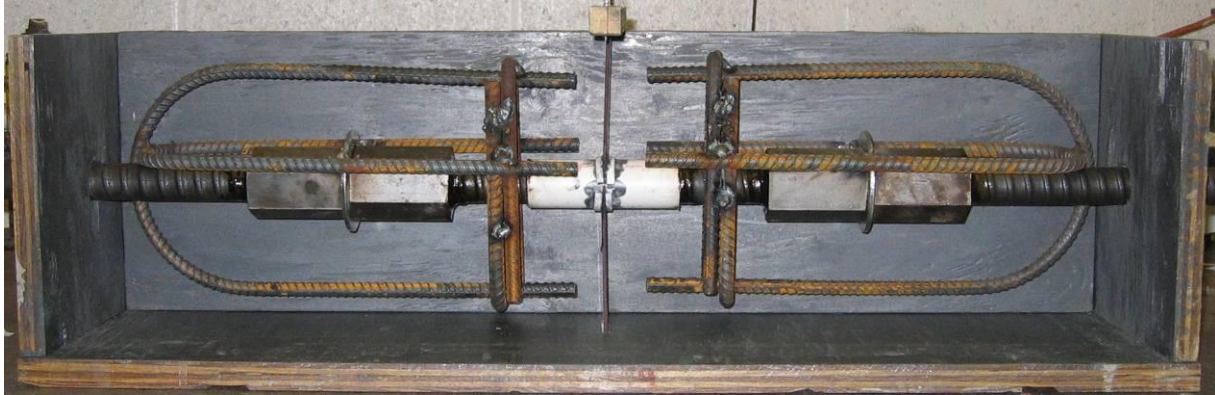


Figure 4-7. Prestressed specimen design



Figure 4-8. Acrylic plate installed in specimen

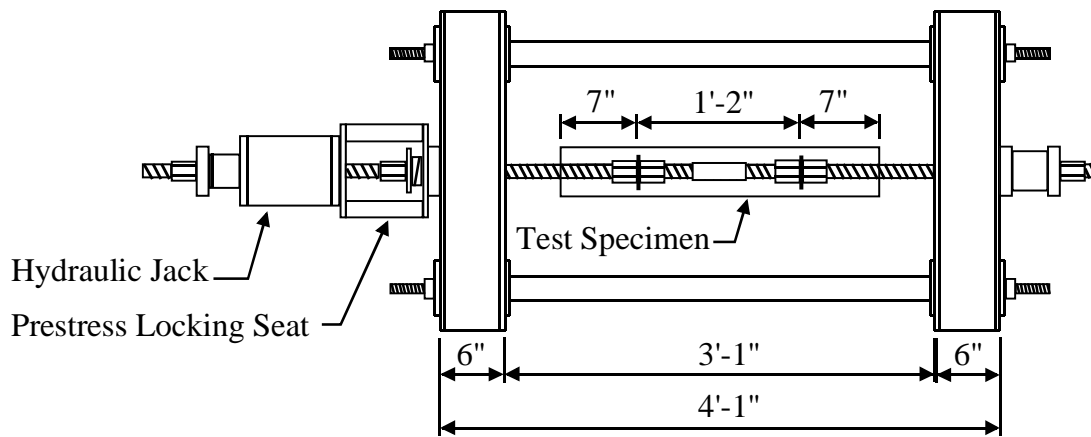


Figure 4-9. Load frame with specimen and instrumentation

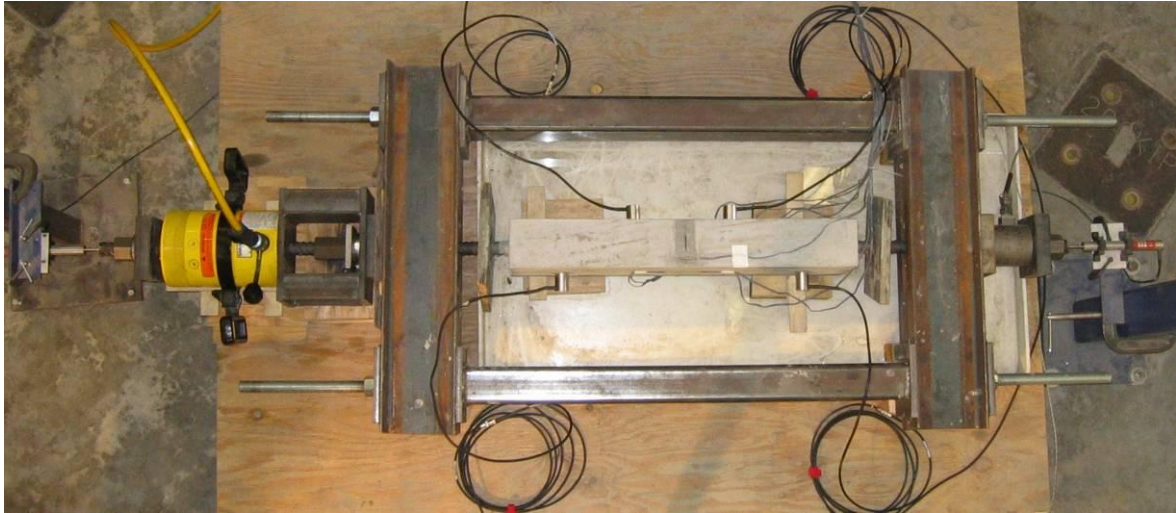
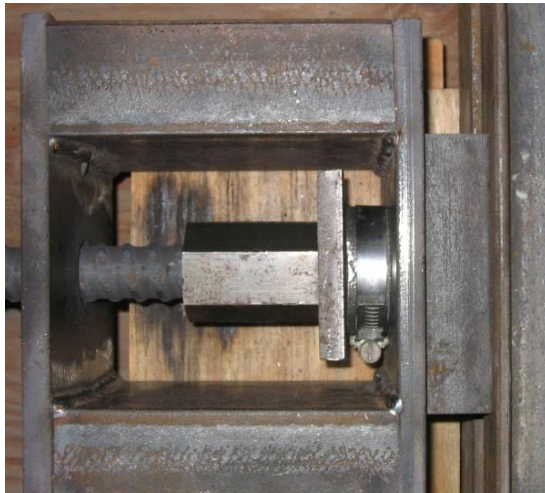
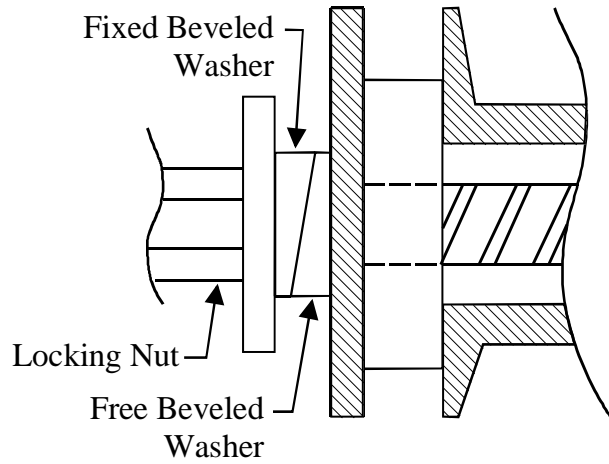


Figure 4-10. Test setup for prestress specimen



A



B

Figure 4-11. A) Top view of prestress locking seat with locking nut and washer setup and B) Side view section of beveled washer and locking nut

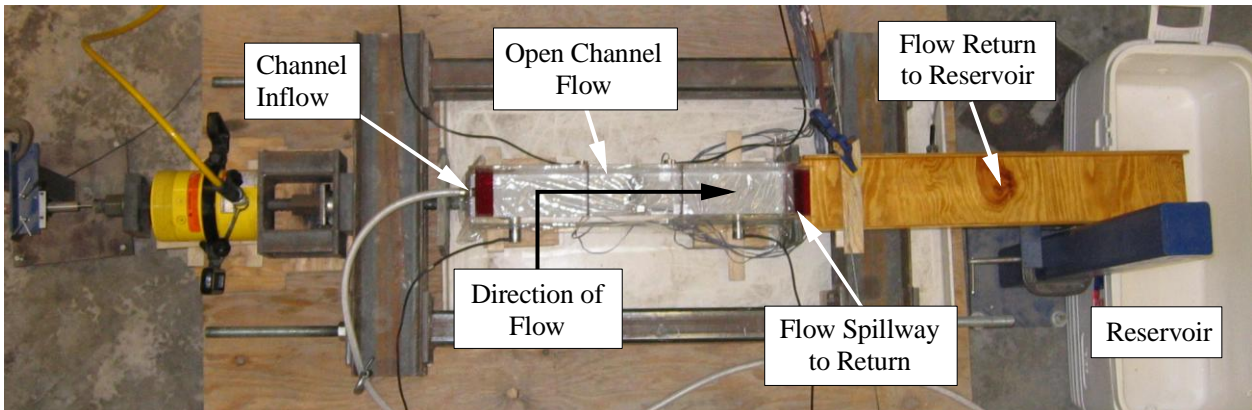


Figure 4-12. Load frame with thermal application setup



Figure 4-13. Load frame with open-channel on thermal test specimen

## CHAPTER 5 INSTRUMENTATION

Each test included instrumentation for load, longitudinal displacement, strain, acoustic emission, and temperature (for thermal specimens). Placement of instrumentation for load, displacement, and acoustic emission (AE) is shown with the test setup in Figure 5-1.

### **Electrical Resistance Concrete Strain Gauges**

Strain gauges were placed to capture both the strain profile and to capture cracking. Gauge locations and nomenclature for the thermal and non-thermal specimens are shown in Figure 5-2. Figure 5-3 shows the staggered placement of gauges R5 through R7 at mid-height of the section. This placement pattern was used to ensure that the primary crack would pass through at least one strain gauge. Nomenclature assigned to the strain gauges was associated with the four faces of the specimen: top, right, bottom, and left (e.g. TOP, R1, BOT, L1).

Strain gauges used in this research were type PFL-20-11-3LT gauges produced by Tokyo Sokki Kenkyujo Co., Ltd. The gauges were foil type electrical resistance, self-temperature compensating (STC) strain gauges with a gauge length of 20mm and temperature compensation number of 11, corresponding to a coefficient of thermal expansion (CTE) of  $11.8 \times 10^{-6} / ^\circ\text{C}$  ( $6.6 \times 10^{-6} / ^\circ\text{F}$ ). Lead wires of the gauges were 3-wire temperature compensating to account for variation in lab temperature during testing.

Strain gauges were applied to the concrete specimen at the midsection prior to testing. The surface of the concrete at the location of the strain gauge was prepared by light grinding and/or sanding to remove concrete laitance. The area was then dusted

with compressed air and cleaned with acetone. Each strain gauge was adhered to the concrete using Loctite 454 Instant Adhesive.

### **Thermocouples**

Type T thermocouples were embedded in the concrete to measure the temperature profile at the midsection of the specimen as shown in Figure 5-4. Thermocouples were spaced through the depth of the specimen, as shown in Figure 5-5, to capture the nonlinear thermal gradient. Spacing ranged from 0.5 in. at the top, where the gradient was most severe, to 2 in. at the bottom. The thermocouple array was placed at 0.75 in. from the outside face of the specimen to avoid interference with the acrylic plate and steel bar. The Type T thermocouples used were Omega #FF-T-20-SLE.

### **Load Cells**

A single load cell at one end of each load frame measured the load applied by the hydraulic jack to the DYWIDAG bar and specimen, as shown in Figure 5-6. Load cells used in this research were Houston Scientific 200 kip load cells. Load was applied using an Enerpac 60 ton hydraulic jack in combination with an Enerpac 10,000 psi hydraulic manual pump.

### **Linear Variable Displacement Transducers**

Linear variable displacement transducers (LVDTs) were placed on each end of the DYWIDAG bar. LVDTs were fixed to stands mounted on the floor to measure the longitudinal tip displacement at each end of the DYWIDAG bar (Figure 5-1). The difference in displacements was then used to calculate the net change in length of the bar. The LVDTs used in this research were of the DCTH Series produced by RDP Electrosense and had a physical range of  $\pm 0.5$  in.

## **Data Acquisition System**

National Instruments model SCXI-1000DC Data acquisition (DAQ) System was used to acquire data from the instrumentation. The DAQ system recorded data from each strain gauge, thermocouple, LVDT, and load cell channel at a frequency of 10Hz. The load cell signal was split between the National Instruments DAQ system and the acoustic emissions DAQ to enable cross-platform synchronization.

## **Acoustic Emissions**

This section provides background information on the nondestructive testing (NDT) approach of monitoring acoustic emission (AE) of a structural member (O'Neill 2009). It also discusses the nature of the data measured, relevant terminology, and how AE data were used to assess damage progression in the prestressed concrete specimens tested in this research.

### **Background Information and Motivation**

Acoustic emission (AE) techniques began in Germany in 1950 with testing of metals by J. Kaiser. AE technology was later modified to be used as a structural integrity monitoring device with concrete. The AE technique has been used as a nondestructive structural monitoring tool for plain concrete (Nielsen and Griffin 1977), reinforced, and prestressed concrete beams under flexural monotonic and cyclic loading conditions (Shield 1997). Detection and location of microcracking and macrocracks has also been successfully completed under flexural loading (Labuz et al.. 2001). AE signal characteristics have also been identified in order to classify the type of damage, microcracking or bond degradation between concrete and steel, that is occurring in reinforced concrete beams (Oh et al. 2000). The successful application of AE

techniques to monitor concrete structural health was the motivation to utilize it as a tool for this research.

## **Introduction**

An acoustic emission is produced when energy is released from a material under stress in the form of a transient stress wave. The cause of the energy release is a change of state of the material such as a crack forming in concrete or bond degradation between concrete and steel. The elastic wave travels through the specimen and is detected by mounted piezoelectric sensors that develop a voltage in response to mechanical stress, which is recorded with a data acquisition system. The output signal contain feature data; amplitude, energy, duration, rise time, and count associated with each “hit” recognized by the sensors. A hit occurs when the amplitude of the electromotive force generated by the sensor rises above a predetermined threshold. The threshold is set to eliminate noise caused by sources other than a structural defect, like electrical interference or ambient sound. A sample waveform from a hit is shown in Figure 5-7.

An “event” is defined as a local material change giving rise to acoustic emission (ASTM E-1316). An event is distinct from a “hit” which is simply the process of detecting and measuring an AE signal on a channel. To record events, hit data from at least two channels must be utilized. Linear interpolation is performed between the coordinates of two sensors based on differences in the arrival times of the first two hits in the event. To observe events, an Event Data Set needs to be programmed into the software performing the analysis of AE feature data. An Event Data Set includes physical characteristics such as; wave velocity through the material; event definition value (EDT); and event lockout value (EVT). EDT is the length of an event in distance units,

physically the distance between AE sensors. The length is later converted to time using the wave velocity. EVT is also a distance but it is what controls the interval between consecutive events. Using an EVT that is larger than EDT could potentially allow hits to be ignored after an event. This might be desirable if reflections of a wave were to generate extraneous acoustic signals that do not constitute useful information.

### **Structural Assessment Techniques**

A key aspect in successfully using AE testing techniques involves identifying the appropriate parameters to focus on within the AE signal data. Energy analysis has previously been found to be a viable means of assessing AE signals for concrete bridge beams (Colombo et al. 2005) and compression of concrete (Puri and Weiss 2006). For the monotonically loaded concrete specimens tested in this research, focus was given to comparing cumulative event energy to applied load to gain insight regarding the damage progression of the prestressed concrete specimen.

### **Acoustic Emission Instrumentation**

The AE equipment utilized in this research was the DISP-16 channel Acoustic Emission System designed by Physical Acoustics Corporation. The system is shown in Figure 5-8. The system features a Windows-based software package, AEWIn, that allows acquisition and replay of collected AE data. The piezoelectric sensors used were model R31-AST with an integrated preamp (Figure 5-9). This sensor was engineered to attain high sensitivity and have the capability to drive long cables without the need for a separate preamplifier. The sensors also contained an integrated auto sensor test (AST) capability that allowed them to pulse elastic energy waves, as well as receive elastic energy waves. The AST feature permits verification of sensor coupling to the specimen of interest. Sensor coupling to the specimen was completed using hot glue as the

adhesive. This sensor model is frequently used for structural health monitoring of small to medium concrete structures.

AE sensors were placed on each specimen at the intervals specified in Figure 5-1 and Figure 5-10. Sensors S1 and S2 were placed on the designated right face and sensors S3 and S4 on the opposite, or left, face of the specimen. The sensors were placed to allow for the capture and isolation of acoustic emission around both the anchors and the area of cracking at midsection of the specimen.

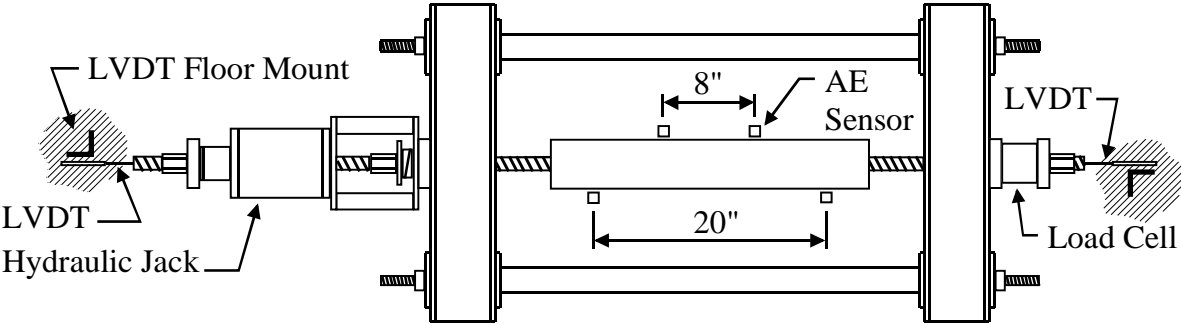


Figure 5-1. Instrumentation setup

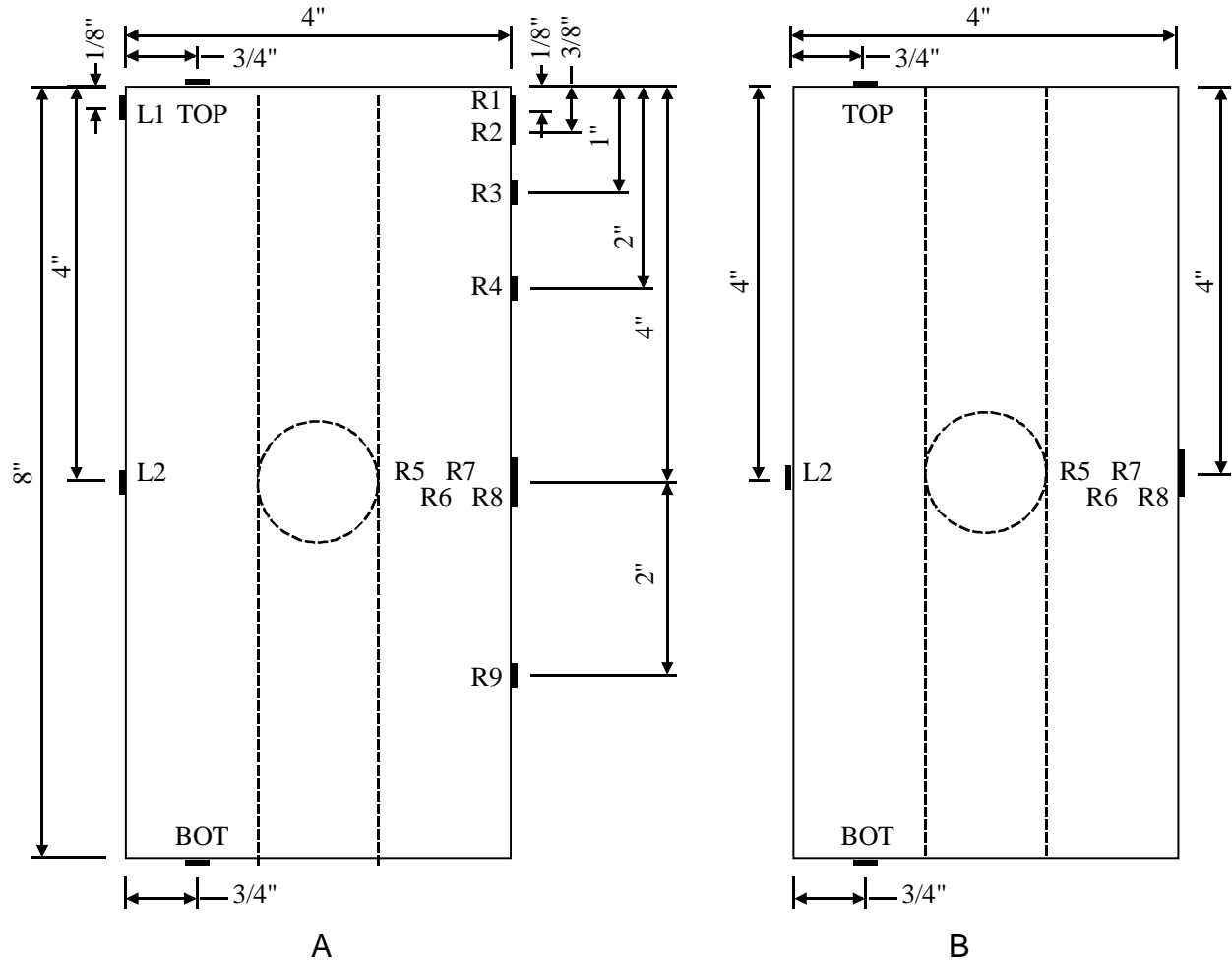


Figure 5-2. Strain gauge location and nomenclature for the A) prestressed thermal specimen and B) prestressed non-thermal specimen

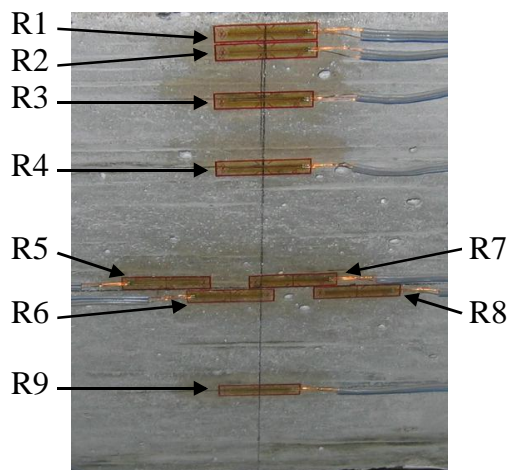


Figure 5-3. Strain gauge placement on right face of prestressed thermal specimen

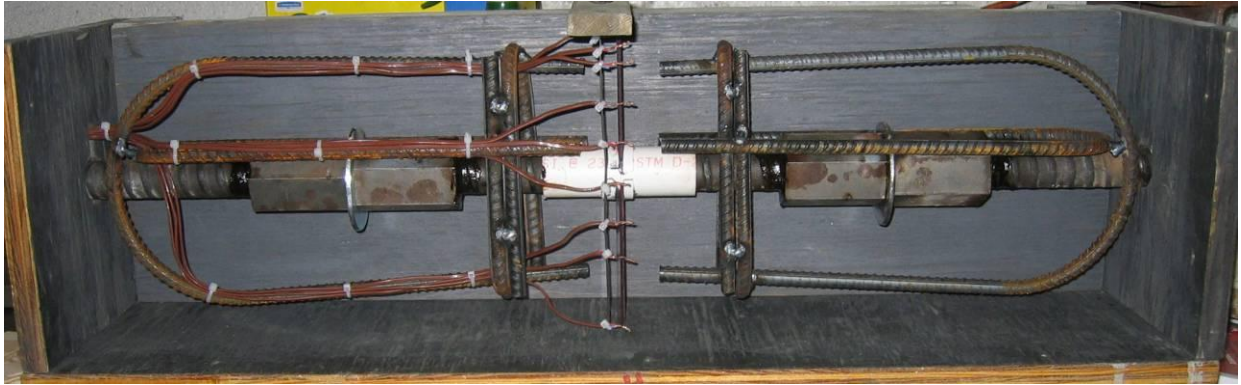


Figure 5-4. Prestressed thermal specimen assembled in formwork

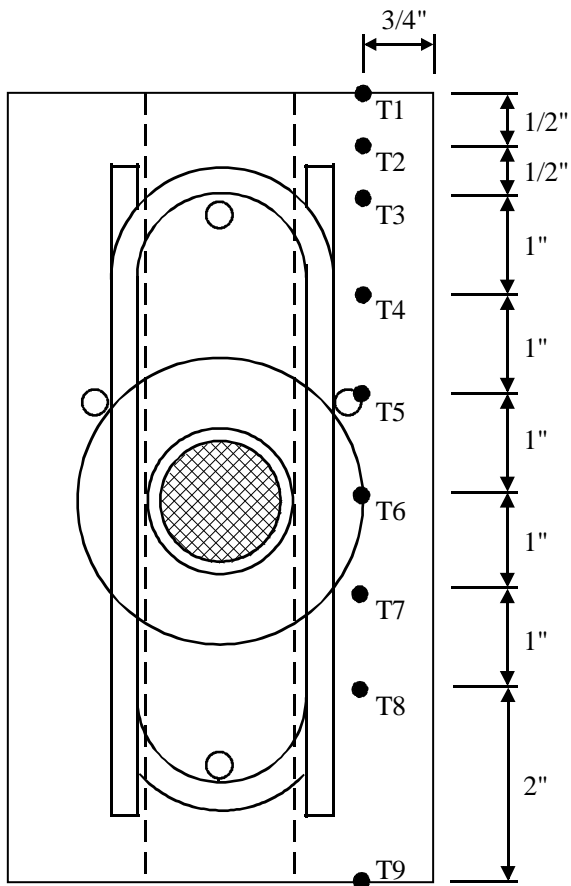


Figure 5-5. Thermocouple locations and nomenclature for prestressed thermal specimen



A



B

Figure 5-6. Applied load measure by A) load cell and applied by A) hydraulic jack

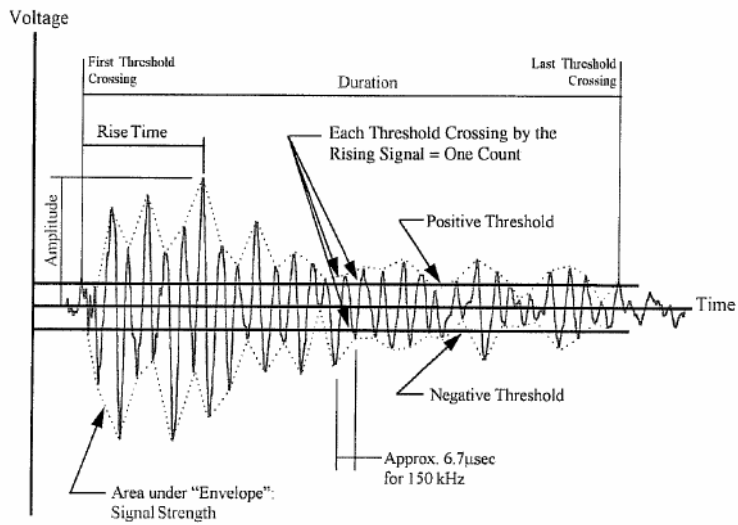


Figure 5-7. Waveform generated by a sensor “hit” (O’Neill 2009)

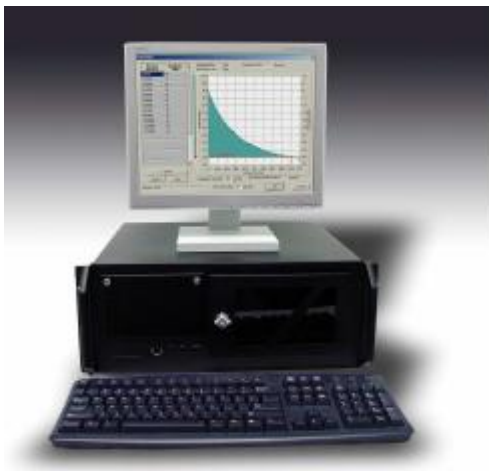


Figure 5-8. DISP-16 Channel Acoustic Emission System (O'Neill 2009)



Figure 5-9. R31-AST Piezoelectric Sensor (O'Neill 2009)

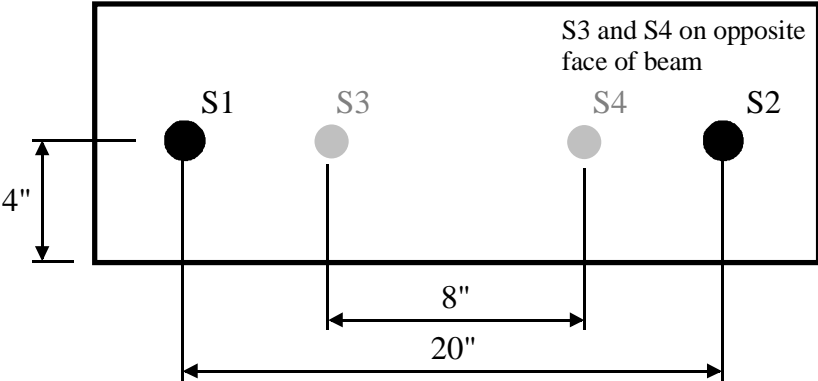


Figure 5-10. Acoustic Emissions sensor placement and nomenclature

## CHAPTER 6 TEST PROCEDURE

Specimen construction and testing extended over a period of several days and included prestressing, concrete mixing and placement, prestress transfer, thermal application, and finally direct tensile loading until cracking. Two identical load frames (Figure 6-1) were used in a single test set so that the same concrete mixture could be used in non-thermal and thermal testing scenarios. Non-thermal and thermal test results were then compared to determine the relative effect of the thermal gradient on cracking behavior.

The test procedure was designed to simulate the stress states in the top flange of a segmental box girder under prestressing, applied loads, and self-equilibrating thermal stresses. After the specimens were cast and prestressed, the resulting stress state is shown in Figure 6-2A. This was intended to represent the precompressed tensile zone in the full scale SRB Bridge segment under prestress alone. To simulate tensile stresses caused by negative bending, the DYWIDAG bar was loaded in tension as shown in Figure 6-2B until the section cracked. For the specimen with the nonlinear thermal gradient imposed, the self-equilibrating stress profile shown in Figure 6-2C was also present. The combination of flexural tension and thermal stresses result in the stress state shown in Figure 6-2D.

### **Prestressing**

To prestress the specimen, the DYWIDAG bar was tensioned against the load frame before concrete placement. With the specimen formwork in place, the stressed bar was locked off using the prestress locking seat assembly. This allowed for the load frame with the specimen to be moved for concrete placement and maintain the

prestress load during curing. Prestressing of the DYWIDAG bar was performed for two load frame assemblies. During stressing of the bar, data acquisition recorded the applied load and longitudinal displacement of the bar. These data were used to determine the initial prestress and prestress loss associated with locking off the bar.

### **Concrete Placement**

For each test set, a single batch of concrete was mixed to ensure consistent mechanical and thermal properties between the non-thermal and thermal specimens. To ensure consistency, coarse aggregates were soaked in water for a 24hr period prior to mixing. The fully saturated aggregates were then removed from the water, allowed to drain for approximately 45 minutes, and then transferred and weighed in sealed buckets. Samples were taken and the aggregate moisture content obtained according to ASTM C566 (2004). During mixing of the concrete, a slump test was performed in accordance with ASTM C143 (2008) to ensure that target slump was reached. For further quality control, the unit weight of the mix was obtained in accordance with ASTM C138 (2009). Nine 4x8 in. cylinders were cast for compressive strength tests, ASTM C39 (2001). The 4x8 in. cylinders were used in lieu of 6x12 in. cylinders due to limited volume of the concrete mixer available. Three 4x4x14 in. beams were cast for the modulus of rupture test, ASTM C78 (2008). The compressive strength test and modulus of rupture test were performed immediately after testing of the non-thermal and thermal specimens were complete.

The concrete mixture was placed into the formwork for each specimen after prestressing of the bars. To provide adequate consolidation of the concrete, each load frame assembly with the specimen was placed on a vibration table. Each specimen was moist cured by covering the specimen with moist cotton towels and plastic sheeting.

The towels were moistened regularly while the specimen cured for 2 days before removing formwork.

### **Non-Thermal Test**

Testing of the non-thermal specimen was conducted on day five as shown in the sequence of stages in Table 6-1. Data were acquired from all instrumentation during this entire test period including just before prestress transfer. The reading taken before prestressing constituted the zero strain reading.

During prestress transfer it was necessary to increase the bar force slightly to allow the beveled washer to be tapped out from under the locking nut and plate (Figure 4-11). This allowed the locking nut to be loosened and the prestress to be transferred to the concrete specimen. The increase in bar force caused a slight tension in the concrete section of approximately 25 microstrain. Careful observation during and after testing determined that this tensile strain was not significant enough to cause damage to the concrete.

Immediately after prestress transfer, tension was applied to the DYWIDAG bar at a rate of approximately 30 kips/min. When cracking of the specimen was visually observed, failure of the prestressed concrete specimen was considered to have occurred and the test was terminated.

### **Thermal Test**

The thermal test procedure was similar in sequence to that of the non-thermal test, with the exception of additional stages for the thermal application (Table 6-2). The procedures for data acquisition, unlocking the stressed DYWIDAG bar, and prestressing of the concrete specimen were identical to that of the non-thermal test. After prestress transfer, a direct tensile load of approximately two-thirds the prestress was applied,

which resulted in a net compressive stress in the concrete. At this point application of the nonlinear thermal gradient was initiated. After initiation of the thermal gradient, direct tensile loading continued such that cracking coincided with the complete development of the nonlinear thermal gradient. Failure of the specimen was considered to have occurred when visible cracking was observed. Upon cracking, the test was completed and data acquisition terminated. Crack pattern and location were then documented for the tested specimen.

Table 6-1. Sequence of stages for prestressed non-thermal specimen

Sequence of stages	Day performed	Duration
1. Tension DYWIDAG bar and lock-off	Day 1	5 minutes
2. Cast concrete in specimen forms	Day 1	1 hour
3. Remove formwork and apply strain gauges	Day 3	n/a
4. Begin data acquisition and take zero reading	Day 5	n/a
5. Unlock and release bar (prestress specimen)	Day 5	2 minutes
6. Apply tensile load to prestressed specimen until cracking observed	Day 5	5 minutes
7. Terminate data acquisition	Day 5	n/a
8. End Test	Day 5	n/a

Table 6-2. Sequence of stages for prestressed thermal specimen

Sequence of stages	Day performed	Duration
1. Tension DYWIDAG bar and lock-off	Day 1	5 minutes
2. Cast concrete in specimen forms	Day 1	1 hour
3. Remove formwork and apply strain gauges	Day 3	n/a
4. Begin data acquisition and take zero reading	Day 5	n/a
5. Unlock and release bar (prestress specimen)	Day 5	2 minutes
6. Apply tensile load to prestressed specimen to 2/3 of total prestress (preload specimen)	Day 5	1 minutes
7. Begin thermal loading	Day 5	2 minutes
8. Continue tensile loading of specimen until cracking observed	Day 5	2 – 3 minutes
9. Terminate data acquisition	Day 5	n/a
10. End Test	Day 5	n/a



Figure 6-1. Load frame assembly prior to concrete placement

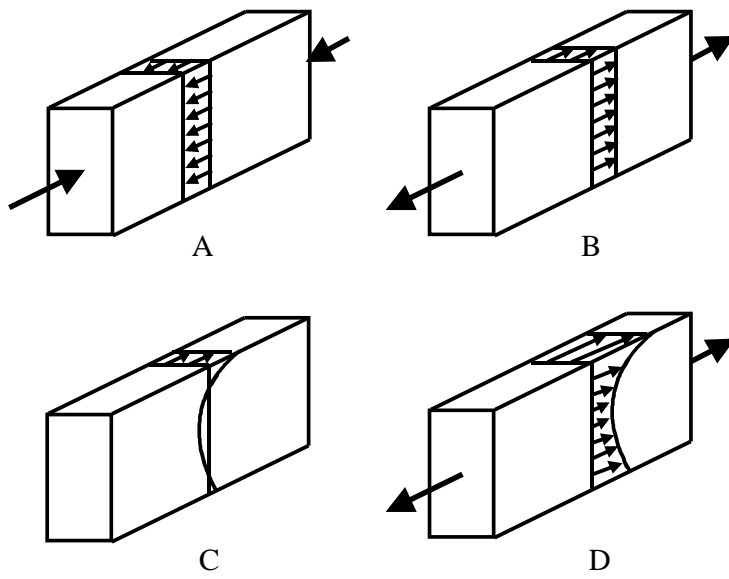


Figure 6-2. Stress state of each stage: A) prestress, B) direct tensile loading, C) self-equilibrating thermal stress, and D) combined thermal and direct tensile loading

## CHAPTER 7 RESULTS AND DISCUSSION

A series of six test sets, Test A through Test F, were conducted. The objective was to determine the effect of an applied nonlinear thermal gradient on the cracking behavior of the concrete specimen relative to a specimen that had no thermal gradient applied. This chapter presents and discusses the results of these tests.

### **Thermal Gradient and Self-Equilibrating Strain**

Tests were conducted to match the upper portion of the AASHTO negative thermal gradient from the SRB Bridge with that of the tested concrete specimens. In these tests, the target temperature at the top surface was maintained at  $-12.3^{\circ}\text{F}$  (relative to the baseline specimen temperature) as the temperature gradient developed through the depth of the specimen to match the AASHTO gradient. The problem encountered with this approach was that the upper portion of the AASHTO negative thermal gradient on the test specimen resulted in lower self-equilibrating strains compared to those predicted in the SRB Bridge. This was due to the shallower test specimen and reduced temperature-profile nonlinearity. It was therefore determined that the target surface temperature of  $-12.3^{\circ}\text{F}$  would be obtained but that the target gradient would be based on the maximum self-equilibrating strain observed. The ability to reach the target gradient was assessed in preliminary testing and the time required to obtain the maximum self-equilibrating strain determined. The target gradient during production testing was then obtained by imposing the thermal application for a set period of time. Direct tensile loading then occurred simultaneously such that the estimated cracking load was reached in conjunction with formation of the target thermal gradient.

Figure 7-1 shows the temperature and strain results of the thermal gradient test. The top surface temperature differential obtained was  $-11.8^{\circ}\text{F}$  at 3.5 minutes and  $-12.5^{\circ}\text{F}$  at 5 minutes after initiating application of the thermal gradient. This compares well with the target AASHTO negative thermal gradient of  $-12.3^{\circ}\text{F}$  and was inline with the time required to load the specimen to cracking.

The thermal gradient and self-equilibrating strain profile are shown through the elevation of the SRB Bridge in Figure 7-2. The test specimen gradients are shown overlaid in the top 8 in. of the profiles. The thermal gradient imposed during specimen testing resulted in a maximum self-equilibrating strain of 65 microstrain at the end of the test (Figure 7-1B) as compared to the SRB Bridge with the AASHTO negative thermal gradient having a calculated peak self-equilibrating strain of 44 microstrain.

Both the measured thermal gradient and resulting self-equilibrating strain gradient obtained on the test specimen were notably more severe than those calculated on the SRB Bridge from the AASHTO negative gradient. Although this is the case, the applied service load component, both in the SRB Bridge and experimental test specimen, is significantly greater than the thermal gradient component of the total strain gradient (Figure 4-2 and Figure 4-3). The total strain profile on the SRB Bridge is predominately a flexural gradient and the strain profile on the experimental test specimen is predominately uniform. The difference between a flexural strain profile and a uniform strain profile can be compared in the modulus of rupture test and the direct tensile test, respectively. Neville noted that the modulus of rupture test, a flexural strain gradient, overestimated the tensile strength of the concrete; the correct value being about  $3/4$  of the modulus of rupture (1995). There were four possible reasons given. The first is due

to assumption based on the elastic beam theory, that the stress-strain relation is assumed linear. The tensile stress block, assumed to be triangular, is in actuality parabolic in shape under loads nearing failure; resulting in a lower maximum fiber tensile stress. Secondly, accidental eccentricity in a direct tensile strength test may result in a lower apparent tensile strength. A third explanation is that in a direct tensile test, the entire specimen volume is placed under the maximum stress, such that the probability of a weak element occurring is high; this is similar to the reasoning of a third-point loading arrangement in the modulus of rupture test. The fourth explanation is that the maximum fiber stress reached may be higher in flexure than in direct tension, this would be due to crack propagation being blocked by less stressed material nearer to the neutral axis of the section. (Neville 1995)

As such, it would be expected that the predicted tensile strength in the SRB Bridge would be greater than the measured tensile strength in the experimental test. The maximum fiber stress measured in the experimental specimen would be  $\frac{3}{4}$  of the maximum fiber stress calculated in the SRB Bridge. The less severe gradient in the SRB Bridge will result in cracking at a higher applied stress than the stress profile applied to the experimental specimen. In addition, there is a  $\frac{1}{3}$  increase of maximum self-equilibrating tensile strain calculated in the experimental specimen compared to the predicted self-equilibrating strain in the SRB Bridge. Thus, the predominantly uniform total strain profile and increased self-equilibrating strain of the experimental specimen produce a harsher condition than those predicted in the SRB Bridge. If any effect was to be seen, it would be seen at a lower applied tensile stress as in the experimental testing.

Strains resulting from the applied mechanical load (prestress and applied tensile load) and strains resulting from the applied thermal gradient combined to form the total measured strain profile of the thermal specimen. Figure 7-3A shows the components of the total measured strain profile on the thermal specimen of Test A. The self-equilibrating strain is calculated from the measured differential temperature gradient. The applied mechanical strain is determined simply by removing the self-equilibrating strain from the total measured strain. This can be compared to the applied mechanical strain measured in the non-thermal specimen shown in Figure 7-3B. There is an observed difference in magnitudes of the mechanical strain component between the thermal and non-thermal specimens of approximately 20 microstrain. One reason for this difference is flexural strain due to unintended bar eccentricity. Another is the presence of residual concrete drying shrinkage strains. These factors, which will be discussed in greater detail later, were not quantified and differences in these factors between specimens in each test set would be expected. The measured compressive strain in the top of the non-thermal specimen at initial cracking can also be associated with the effect of residual concrete drying shrinkage strains that result in a net residual tensile strain.

As discussed, Figure 7-3A shows that the self-equilibrating strain contribution to the total strain is significantly greater than that of the applied mechanical strain in the top portion of the specimen where the self-equilibrating strain profile is most severe. This contribution of self-equilibrating strain validates the reasoning behind needing to consider these strains in design. If the nonlinear thermal gradient does have an effect on the cracking behavior, it can be expected that the contribution from self-equilibrating

strain would control over the mechanical strain contribution. To quantify the effect of the self-equilibrating strain contribution, the non-thermal and thermal specimens were compared.

### Strain – Load Analysis

Strains measured during testing, and discussed below, required two analytical corrections. Although the strain gauges used in testing were self-temperature compensating (STC), an increased level of accuracy of strain measurement was achieved by applying two additional temperature corrections. The first correction accounted for a change in the gauge factor as the temperature deviated from the specified temperature at factory calibration. Murray and Miller (1992) explain that there is an apparent strain resulting from the thermal output associated with this temperature deviation. A factory specified equation for computing the apparent strain produced by this deviation is:

$$\varepsilon_{app} = 2.97 \times 10^{-1} + 2.73 \times T^1 - 7.23 \times 10^{-2} \times T^2 + 5.30 \times 10^{-4} \times T^3 - 1.40 \times 10^{-6} \times T^4 \quad (\mu\varepsilon) \quad 7-1$$

where  $\varepsilon_{app}$  is the apparent strain from thermal output ( $\mu\varepsilon$ ) and  $T$  is the temperature of material at the gauge ( $^{\circ}\text{C}$ ).

A gauge factor of 2.00 was assumed in Equation 7-1. The equation was adjusted to account for the actual gauge factor by applying the following ratio (Murray and Miller):

$$\varepsilon'_{app} = \frac{GF_1}{GF_2} \varepsilon_{app} \quad 7-2$$

where  $\varepsilon'_{app}$  is the corrected apparent strain from thermal output,  $GF_1$  is the gauge factor set for apparent strain (2.00),  $GF_2$  is the gauge factor of strain gauge used, and  $\varepsilon_{app}$  is the calculated apparent strain from thermal output.

The second correction accounted for the difference in the coefficient of thermal expansion (CTE) between the gauge and concrete. The strain gauge was manufactured with a CTE of  $11.8 \times 10^{-6} / ^\circ\text{C}$  ( $6.6 \times 10^{-6} / ^\circ\text{F}$ ) and the concrete had an estimated CTE of  $14.5 \times 10^{-6} / ^\circ\text{C}$  ( $8.0 \times 10^{-6} / ^\circ\text{F}$ ). This final correction resulted in a total thermal output of:

$$\varepsilon_{TO} = \varepsilon'_{app} + (\alpha_2 - \alpha_1) \times 10^6 \times \Delta T \quad 7-3$$

where,  $\varepsilon_{TO}$  is the total thermal output correction ( $\mu\varepsilon$ ),  $\varepsilon'_{app}$  is the corrected apparent strain from thermal output ( $\mu\varepsilon$ ),  $\alpha_1$  is the specified CTE of the strain gauge ( $1/^\circ\text{C}$ ),  $\alpha_2$  is the estimated concrete CTE ( $1/^\circ\text{C}$ ), and  $\Delta T$  is the change in temperature from the initial zeroed strain reading ( $^\circ\text{C}$ ).

The total thermal output correction strain from Equation 7-3 was added to the apparent measured strain to obtain the corrected measured strain. Temperature data used in Equation 7-1 and Equation 7-3 were obtained from thermocouples embedded in the specimen. The temperature gradient was assumed to be uniform through the width of the specimen. Where the elevation of a thermocouple (and therefore temperature data) did not match that of a strain gauge, the thermal output correction was linearly interpolated.

Data from the strain gauge designated "TOP" was not included in the strain profiles shown in Figure 7-3. This was due to uncertainty regarding the temperature of the gauge installed at the interface between the concrete and chilled water flow during thermal loading. An average of strains from the top most gauges on the right and left faces, R1 and L1, respectively, were taken as the top most reading as an alternative to the TOP strain gauge. Strain data on the top surface were linearly extrapolated from the two top most gauges.

## Behavior

During each of the test sets performed, strain data and AE data were measured. A representative set of typical results (from Test A) are shown in Figure 7-4 and Figure 7-5. In these figures, the load axis indicates the tension load applied to the DYWIDAG bar. Recall that the concrete specimen was prestressed (i.e., precompressed) at the beginning of this load test. Throughout this discussion, the sign convention is such that applied tensile load is considered positive. Strain values are net measured strains relative to an initial reading taken with no prestress or applied load. The strain sign convention is such that tensile strain is positive and compressive strain is negative. Cumulative AE energy is also plotted. The AE feature event energy is the total elastic energy released by an emission event (ASTM E-1316 2006). The AE cumulative event energy is the sequential summation of energy from each event, starting at the onset of loading.

The initial measured strain of approximately -170 microstrain to -250 microstrain at zero applied tensile load is due to the prestress (Figure 7-4 and Figure 7-5). If the prestressing were applied uniaxially, then the strains in all of the gauges should be equal. Variation in the initial measured strain, however, indicates that the prestressing was applied with some eccentricity, which induced flexural strain. The flexural strain contribution to the measured strain varies with the location of each strain gauge in relation to the neutral axis of the section. Because the magnitude and distribution of the initial strain is similar between the thermal and non thermal specimens, it is likely that the DYWIDAG bar and internal anchors were not perfectly centered or parallel, resulting in induced flexure. Minimal out-of-straightness in the DYWIDAG bar while stressed prior

to curing of the concrete specimen also may have contributed to the flexural strains when the specimen was prestressed.

As bar tension was increased from zero, the concrete specimen was decompressed. Each strain gauge indicated linear behavior as the strain approached zero with the slopes of the plots varying due to gauge location and eccentric prestressing. Strains in both thermal and non-thermal specimens reached a plateau at approximately 30 kips. In the thermal specimen the sharp increase in strain at approximately 25 kips was due to the application of the thermal gradient. The marked increase in strain, particularly in the top gauge, is associated with the self-equilibrating strains resulting from the nonlinear thermal gradient. No additional load was applied to the specimen for approximately 2 minutes as the thermal gradient was imposed.

The plateau in strain is associated with specimen stress moving from net compression to net tension. Ideally, the strain-load plot would continue from compression to tension without a change in slope. As the stress moved from compression to tension however, there was a small amount of “take up” in the anchorage. This take up was presumed to be the result of minute gaps formed between the anchor face and internal concrete surface from drying shrinkage of the concrete during curing. The anchor traversed this gap as it transitioned from applying a compressive stress on the specimen to applying a tensile stress on the specimen. Additional internal movement may have occurred due to crushing of the concrete at the face of the anchor and debonding of the DYWIDAG bar within the specimen.

Under ideal conditions the strain would have been zero over this transition between net compression and net tension. Drying shrinkage also resulted in residual

shrinkage strains occurring from the fixed conditions between internal anchors. This contributed an initial tensile strain in the concrete before the strain gauges were applied and zeroed.

As loading continued beyond the strain plateau, the specimen was subjected to net tension. The initial tensile slope of the plots are linear over a range of about 10 kips in the non-thermal specimen and 15 kips in the thermal specimen. As loading continued beyond this point, the slope of the plot began to decrease. As noted in both the thermal and non-thermal plots, increased AE activity consistently occurred near this change in slope. While the decrease in slope would be indicative of stiffening, it is thought that this is the result of the reduced effectiveness of the strain gauge as microcracking begins.

Although the strain gauges appeared to indicate stiffening, in reality, the concrete is actually softening due to the microcracking. This is confirmed by the load displacement plot Figure 7-6, which shows the total load in the prestressing bar plotted against the bar elongation as measure at each end of the bar. The plot shows an overall decrease in specimen stiffness due to the microcracking occurring in the concrete. This point is the same as that noted in the load strain plot. The displacement shown is the total elongation of the steel bar measure end-to-end of the total experimental system, including the composite specimen and steel bar extended from each end (Figure 7-8B). The initial prestressing of the steel bar without concrete is shown to be linear in Figure 7-6. After curing and prestressing of the concrete specimen, loading of the specimen is shown to remain linear until initial microcracking occurs (determined using strain-load) and then the stiffness is reduced as cracking of

the specimen progresses. The initial nonlinear portion to 15 kips can be associated with unmeasured initial deformations in the load frame.

The incremental rise and fall of strain evident in the plots resulted from the use of a manual hydraulic jack. After each stroke of the manual hydraulic jack, a slight loss of the applied direct tensile load, and thus strain, was observed on the specimen. This loading pattern did not appear to have any effect on the outcome of testing.

The slope change noted at the initiation of microcracking was typically dependent on the location of the final crack relative to the individual gauge. Generally, data from each strain gauge indicated an increase in axial stiffness when microcracking, and eventually macrocracking, occurred at the location of the gauge. In a few instances, the strain gauge data indicated a decrease in the apparent stiffness. This typically occurred when cracks formed in the vicinity of the gauge but not directly under the gauge. A few atypical instances where the strain gauge did not behave in this manner further indicate a reduced effectiveness of the strain gauge as microcracking begins. These instances may have occurred due to how debonding occurred at the surface interface of the gauge and concrete as microcracking occurred under and around the gauge..

The slope change continued until the microcracking coalesced into a single visible crack crack ( B

Figure 7-7), which occurred at 89 kips and 83 kips for the non-thermal and thermal specimens, respectively. These macrocracks formed suddenly and were detected both visually and audibly. Ultimate failure of the specimen occurred when visible macrocracking and a sharp increase, or decrease, in strain was observed. At failure of the specimen, the minimal difference in the loads between the thermal and non-thermal specimens was noted. Further analysis was performed on the tests to quantify the

differences observed in cracking behavior between the thermal and non-thermal specimens.

### **Analysis**

To determine the share of the load carried by the concrete under net tension, the test specimen was modeled using a spring analogy. Figure 7-8A shows a model of the concrete section and steel bar between the anchors. If the gauge lengths of the concrete and steel bar are equal, then the relative stiffness is a function of the cross sectional area and modulus of elasticity. The total stiffness is the sum of the two stiffness terms. Using the section dimensions, a concrete modulus of elasticity of  $57000\sqrt{f'_c}$ , and a steel modulus of 29,000 ksi, it was determined that the concrete section comprises 83% of the total stiffness while the steel bar contributes 17%, which results in the concrete carrying most of the load applied to the bar.

To determine the net effect of the system stiffness on the overall load-displacement (Figure 7-6), the stiffness of the steel bar outside the anchors must be considered. Figure 7-8B shows the added spring element to account for this additional steel bar length. The calculated stiffness for this spring is 4% of the combined stiffness of the two parallel springs. The added bar length dominates the load deflection behavior because it is in series with the specimen and its stiffness is so much lower than that of the specimen. This explains the relatively small change in slope of the load-displacement plot when the concrete begins microcracking (Figure 7-6).

Figure 7-9 shows an idealized representation of the test data with measured strain plotted on the y-axis. The total bar load measured during the test was converted to stress using the portion of the load carried by the concrete as determined using the

spring analogy model. This load was divided by the section area to obtain stress, which was offset by the known prestress. The net concrete stress,  $f$ , was normalized by the square root of the average cylinder compressive strength for the tested specimen.

Decompression, anchorage take up, and net tension define the three distinctive regions of the stress strain curves for the specimen. Decompression is defined as the load range from the beginning of the test to the plateau associated with take up of the anchorage. Net tension began at the end of the anchorage take up, which is defined as the intersection point of the tangent lines occurring before and after the change in slope. The average of the strain gauges with the highest and lowest strain reading (shown connected by a small dashed line in Figure 7-4 and Figure 7-5) were used to establish the point at which net tension began. The tangent lines, points of intersection, and averages were all determined graphically.

Generally, the initial portion of the net tension curve was linear and as microcracking initiated in the concrete, the curve became nonlinear. The initiation of microcracking was also typically marked by a significant increase in AE cumulative event energy, which also indicates the occurrence of microcracking. The AE cumulative event energy assisted in quantitatively determining the onset of damage to the concrete specimen. It was observed that the rate of accumulation of AE event energy increased sharply at the onset of microcracking, corresponding to the change in apparent axial stiffness of the specimen. This point was determined, using AE data, as the intersection of a tangent line passing through data points that occurred during and after the take up of the anchorage, and a tangent line passing through data points following the sharp increase in accumulation of AE event energy. Accumulation of AE event energy that

occurred prior to the tensile strain region was thought to be associated with events occurring at the bond interface of the DYWIDAG bar and concrete. To eliminate extraneous AE events occurring from movement of the anchorage during loading, only the events occurring between AE sensors 3 and 4 in Figure 5-10 were used.

To evaluate the effect of the imposed self-equilibrating thermal stress on cracking behavior of the section,  $f_i$  and  $f_{cr}$  are defined. Stress  $f_i$  represents the average concrete net tensile stress at which microcracking begins, whereas  $f_{cr}$  is the average concrete net tensile stress required to form a visible crack. Both values are taken as a difference relative to the onset of the net tensile region as previously defined. Typical values of  $f_i$  and  $f_{cr}$ , defined earlier for an idealized data set in Figure 7-9, are presented for a typical test set in Figure 7-10 and Figure 7-11.

### **Cracking Behavior**

To evaluate the effect of the imposed self-equilibrating thermal stress on cracking behavior of the section, the net tensile stress at initial microcracking,  $f_i$ , and the net tensile stress at visible cracking,  $f_{cr}$ , were compared for thermal and non-thermal specimen tests. By specifically investigating  $f_i$  for each thermal and non-thermal test, the effect of the nonlinear thermal gradient on the initiation of cracking behavior was determined. The net tensile stress values were normalized by the square root of the concrete compressive strength and compared. The results of  $f_i$  and  $f_{cr}$  are compared by showing the range of microcracking for each test set in Figure 7-12. Further numeric data represented in this figure can be found in Appendix A.

A direct comparison among non-thermal tests or among thermal tests was not considered due to concrete and test condition variability. The major factors contributing to the variability between tests were concrete material properties per batch (e.g.

concrete compressive and tensile strength) and prestress force. As such, direct quantitative comparisons were considered only between the non-thermal and thermal specimens of a single test set.

In investigating the onset of cracking, it would be expected that the addition of a self-equilibrating tensile strain on a section, if significant, would result in a reduction in the applied net tensile load required to crack the specimen. This would result in a lower applied net tensile stress on the concrete. It can be observed in Figure 7-12 that the lower bound of microcracking,  $f_i$ , of the thermal specimens show no such consistent decrease in applied net tensile stress when compared to the non-thermal specimens. The coefficient of variation for normalized values of  $f_i$  for all tests was 61%, with an average normalized value of  $f_i$  of 3.3 for all tests. This overall variation and the variation in  $f_i$  values for thermal specimens relative to non-thermal specimens reveal that there may be no significant effect that the nonlinear thermal gradient has on the initiation of cracking behavior.

For values of the normalized net tensile stress at cracking ( $f_{cr}$ ), the coefficient of variation for all tests was 31% and the average value for all tests was 13.3. The observed differences in  $f_{cr}$  between non-thermal specimens and thermal specimens were not considered as critical in this investigation compared to the differences in  $f_i$ . The effect of a nonlinear thermal gradient on the serviceability, and thus the *onset* of damage to the concrete in the form of cracking, was the primary focus of this investigation.

The increased range of microcracking observed in Test A compared to other tests could be due to environmental conditions during concrete mixing and curing resulting in

a difference in concrete properties (e.g. modulus of elasticity). Since test specimen results were compared within each test set, this was considered to be a minor factor in the results.

The normalized modulus of rupture for each test set, along with the ACI 318 recommended normalized modulus of rupture at 7.5, are shown in Figure 7-12. The averages for the upper and lower bounds of microcracking are shown for all tests, 3.3 and 13.3, respectively. This compares to the general cracking behavior of concrete previously discussed where it was noted that the normalized modulus of rupture could have a range between 5 and 12 (Popovics 1998). These similar ranges further reveal that there may be no significant effect that the nonlinear thermal gradient has on the cracking behavior of concrete. Rather, cracking behavior influenced by any effect of a nonlinear thermal gradient is dominated by the influence of variability associated with concrete in tension.

With both an observed decrease and increase, compared to an expected decrease, in the normalized net tensile stress at initial microcracking of the thermal specimen relative to the non-thermal specimen; and an observed average range of microcracking similar to that of the typical range for modulus of rupture in concrete; the influence of a nonlinear thermal gradient and the resulting self-equilibrating strains appear to be insignificant. Based on the tests conducted in this study, it has been determined that the self-equilibrating stresses from nonlinear negative thermal gradient had no discernable influence on the cracking behavior of concrete specimen tests in this research. As such, the consideration of a nonlinear thermal gradient and the structural

response to such a gradient as outlined by AASHTO (1999) may not need to be considered for serviceability.

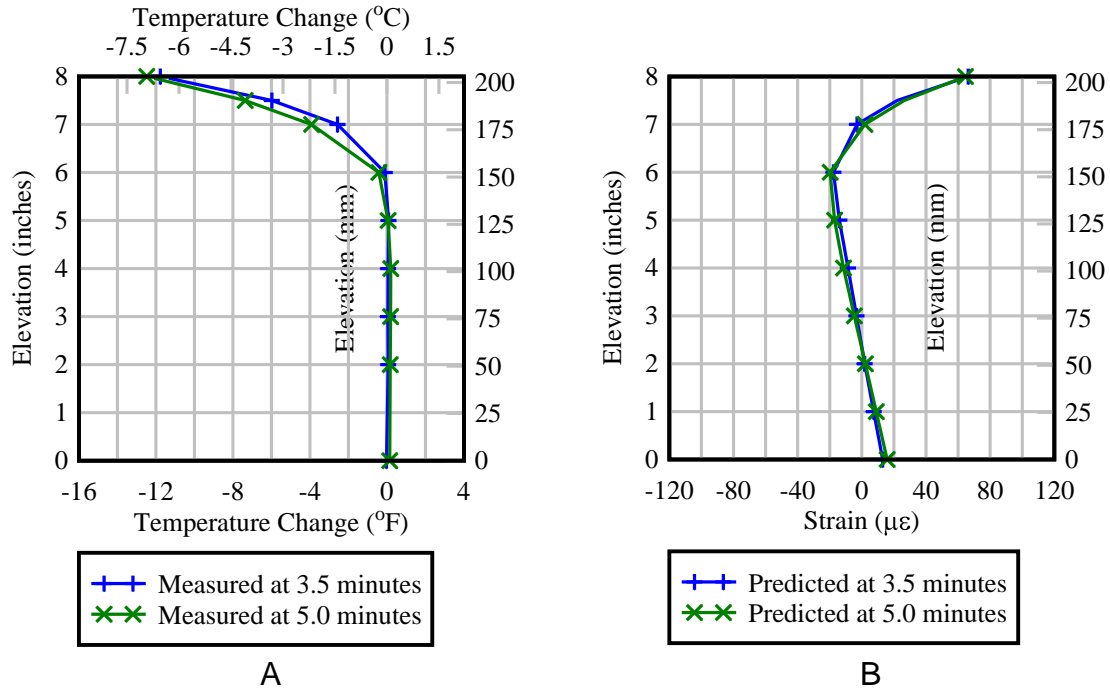


Figure 7-1. Test A – A) measured thermal gradient and B) calculated self-equilibrating strain gradient

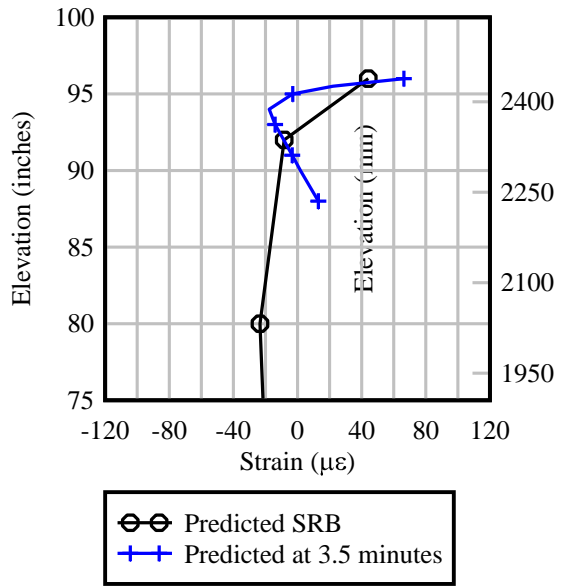
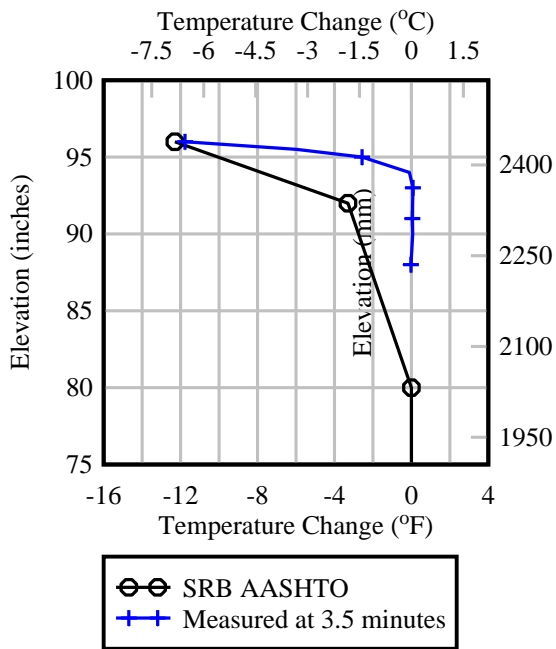


Figure 7-2. Test A and SRB comparison of A) thermal gradients and B) self-equilibrating strain gradients

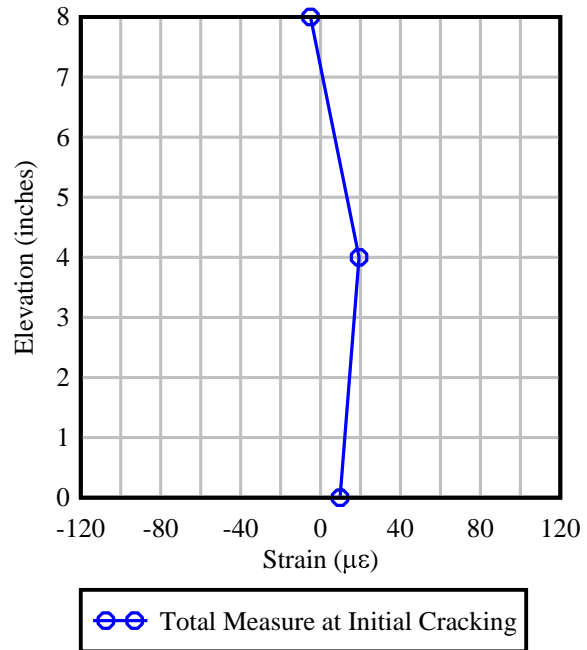
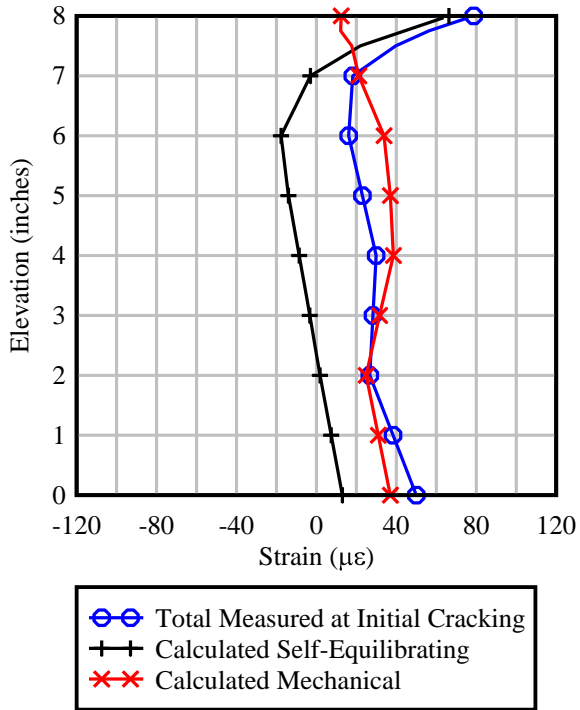


Figure 7-3. Test A measured strain components from A) thermal specimen and B) non-thermal specimen

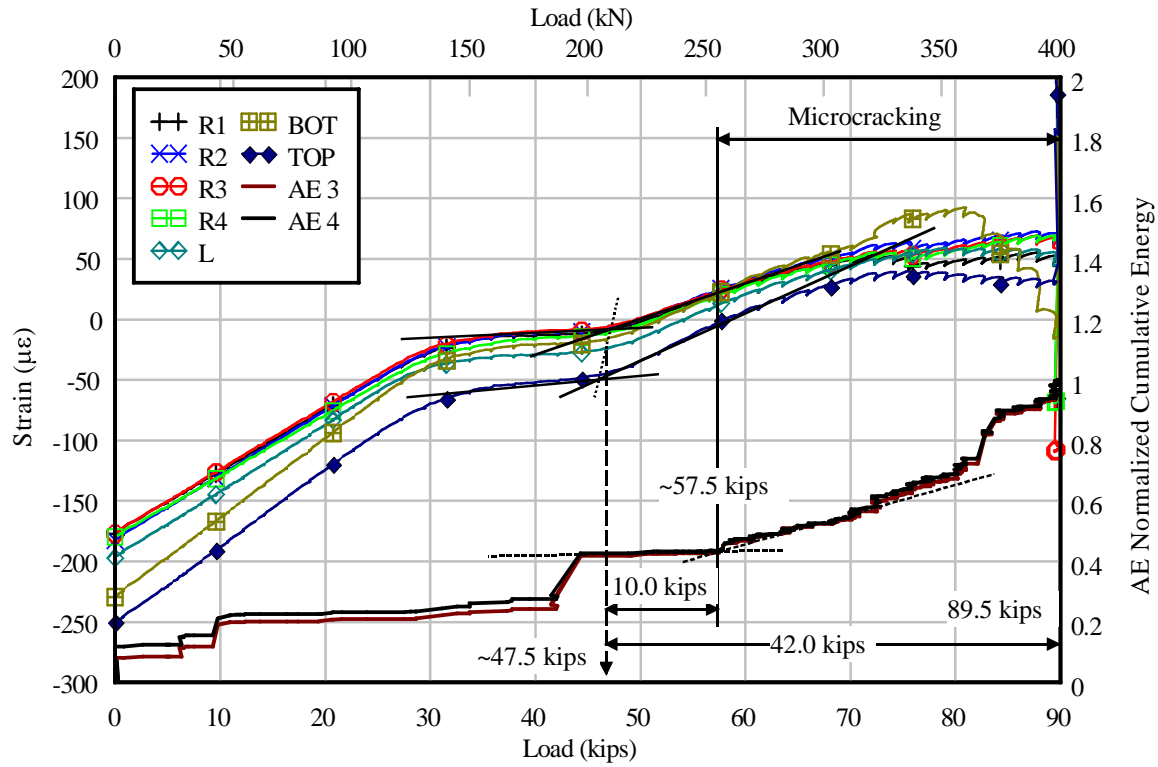


Figure 7-4. Test A - Non-thermal specimen

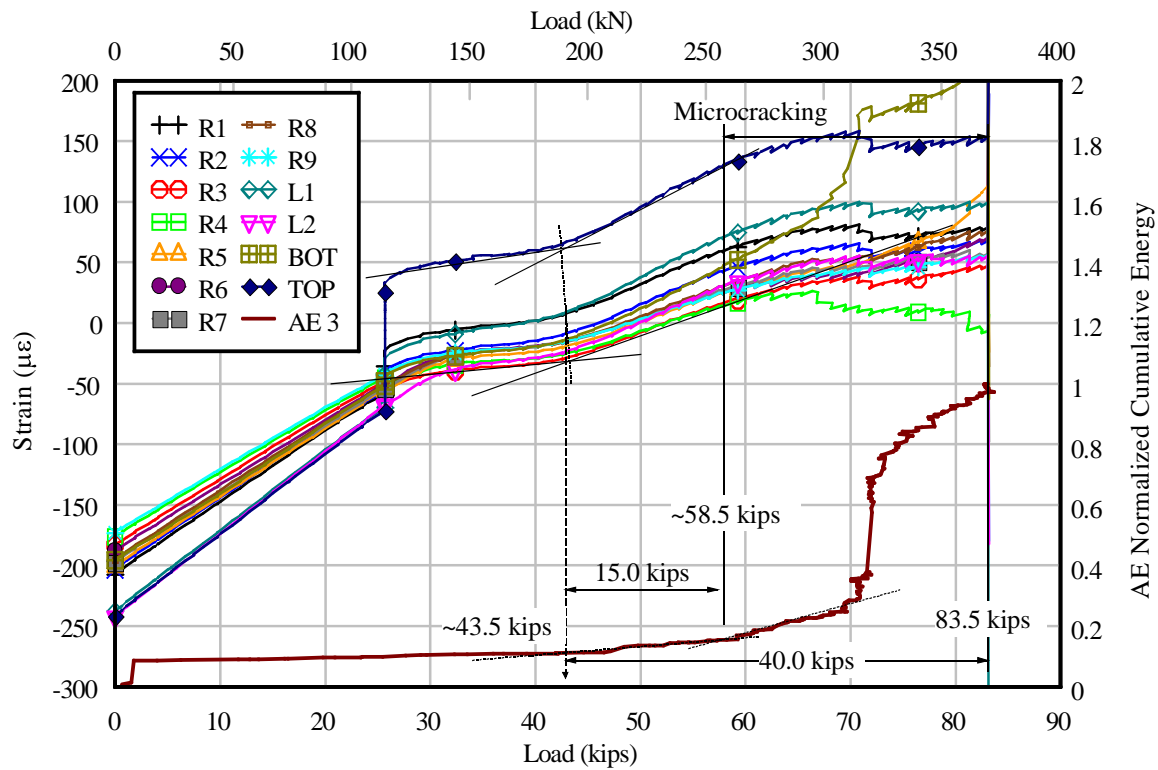


Figure 7-5. Test A - Thermal specimen

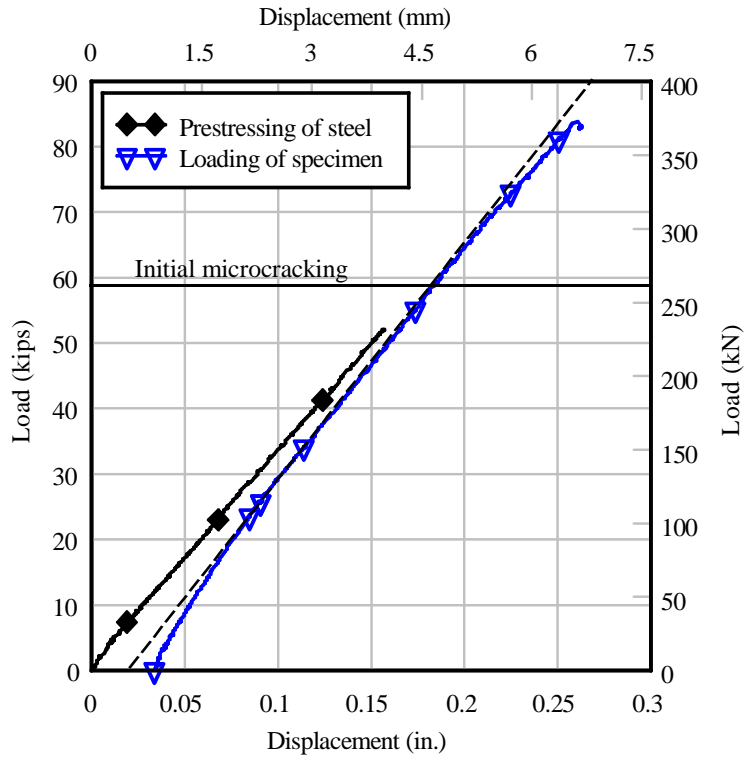


Figure 7-6. Test A Load-Displacement of Thermal specimen

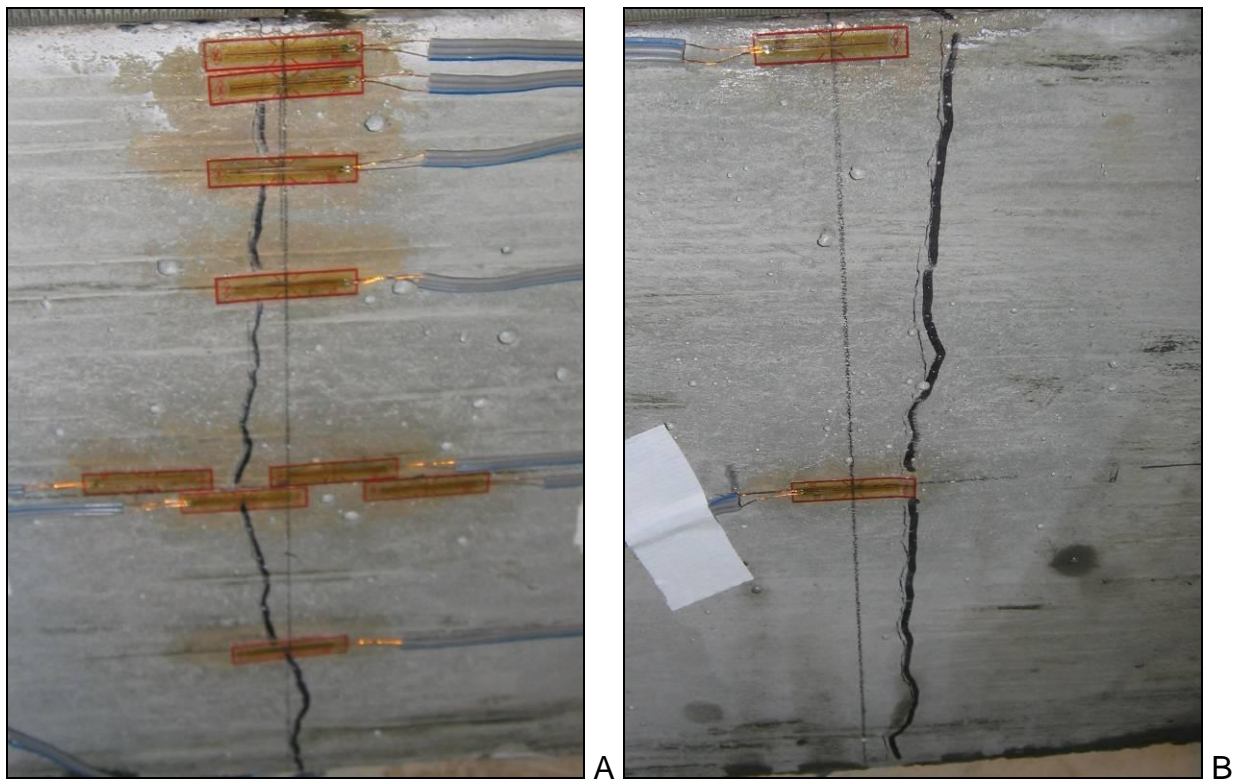
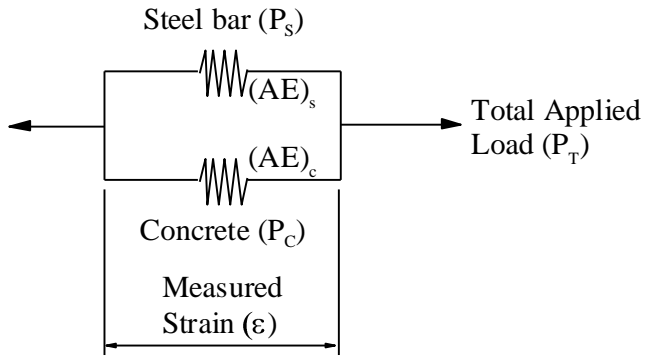
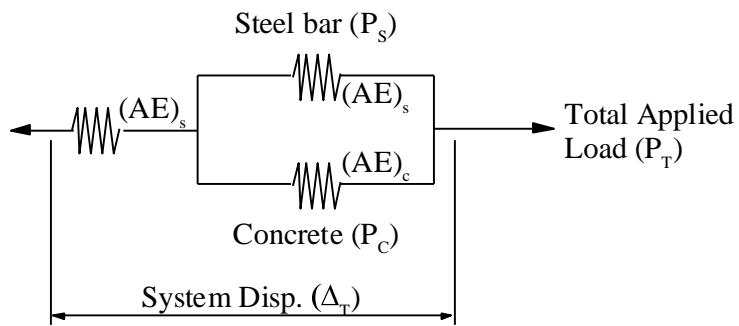


Figure 7-7. Test A - Crack on A) right face and B) left face of thermal test specimen



A



B

Figure 7-8. Axial stiffness of A) specimen and B) system

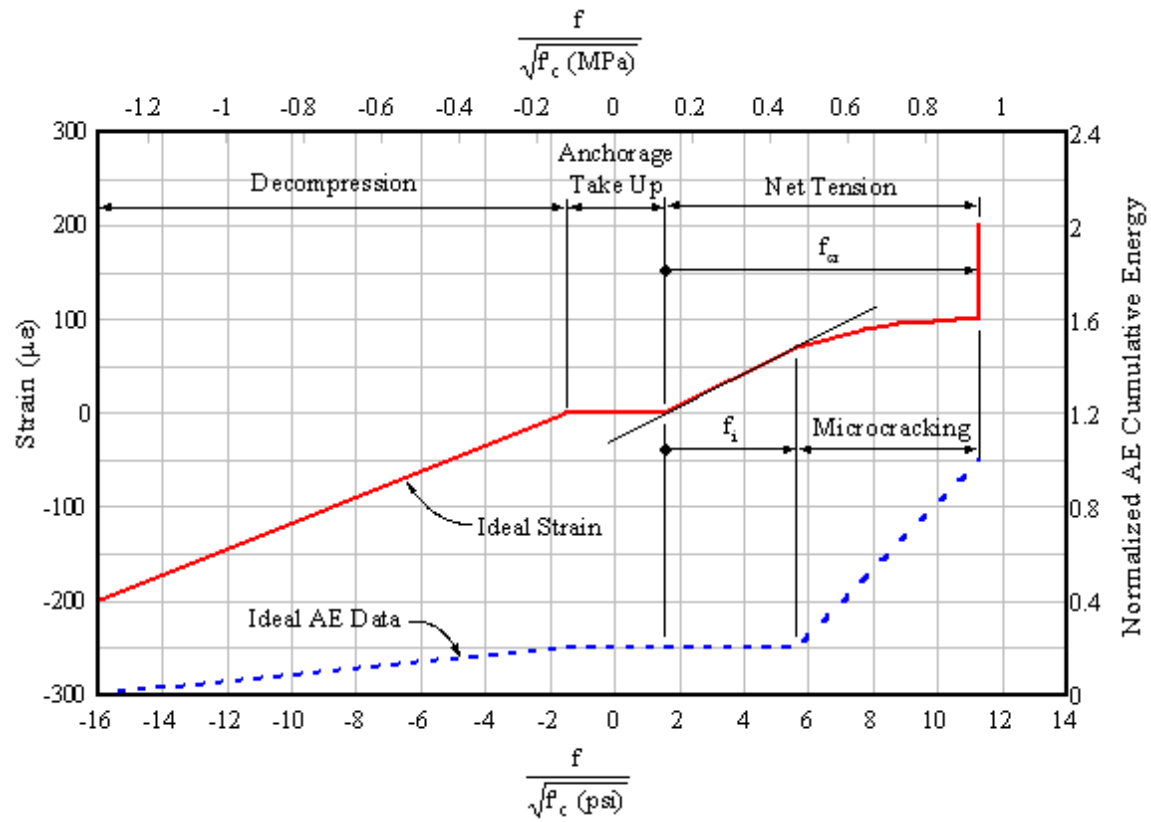


Figure 7-9. Idealized test data set and terminology

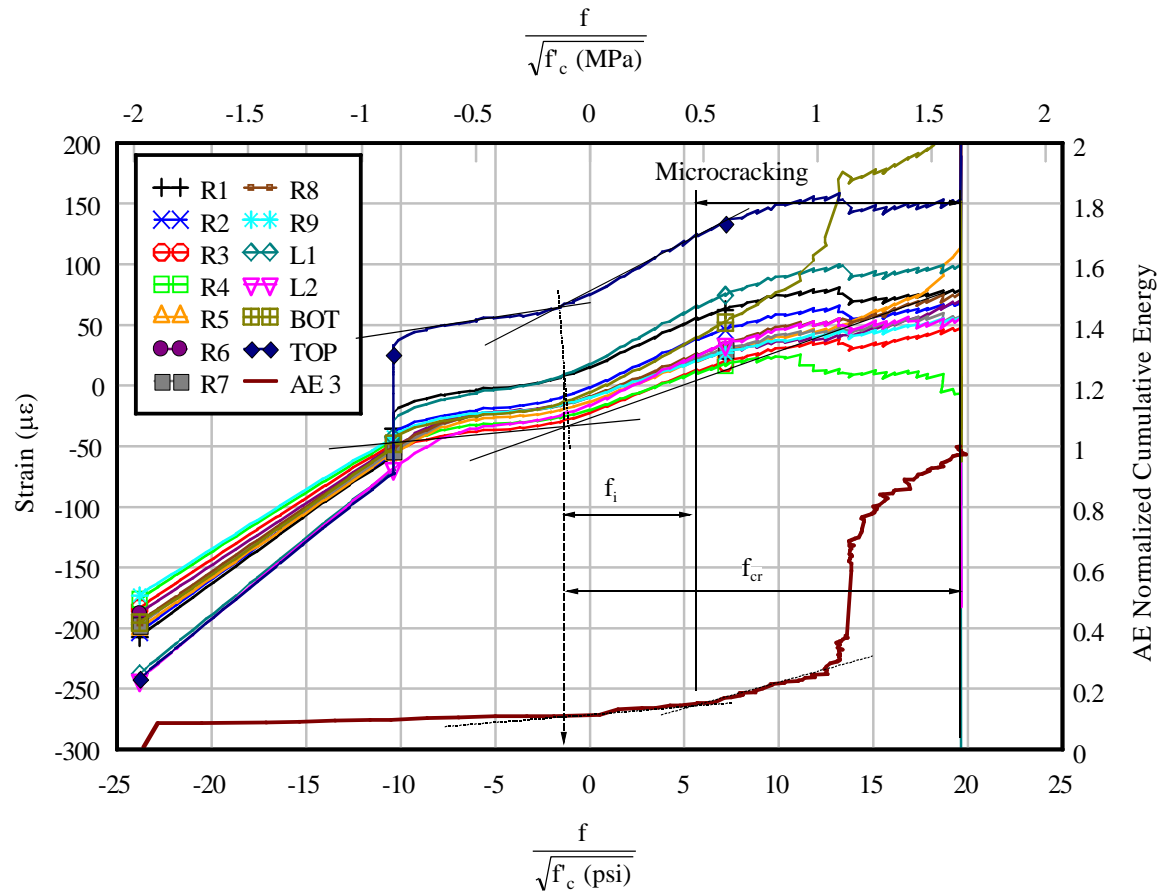


Figure 7-10. Test A - thermal specimen (stress ratio)

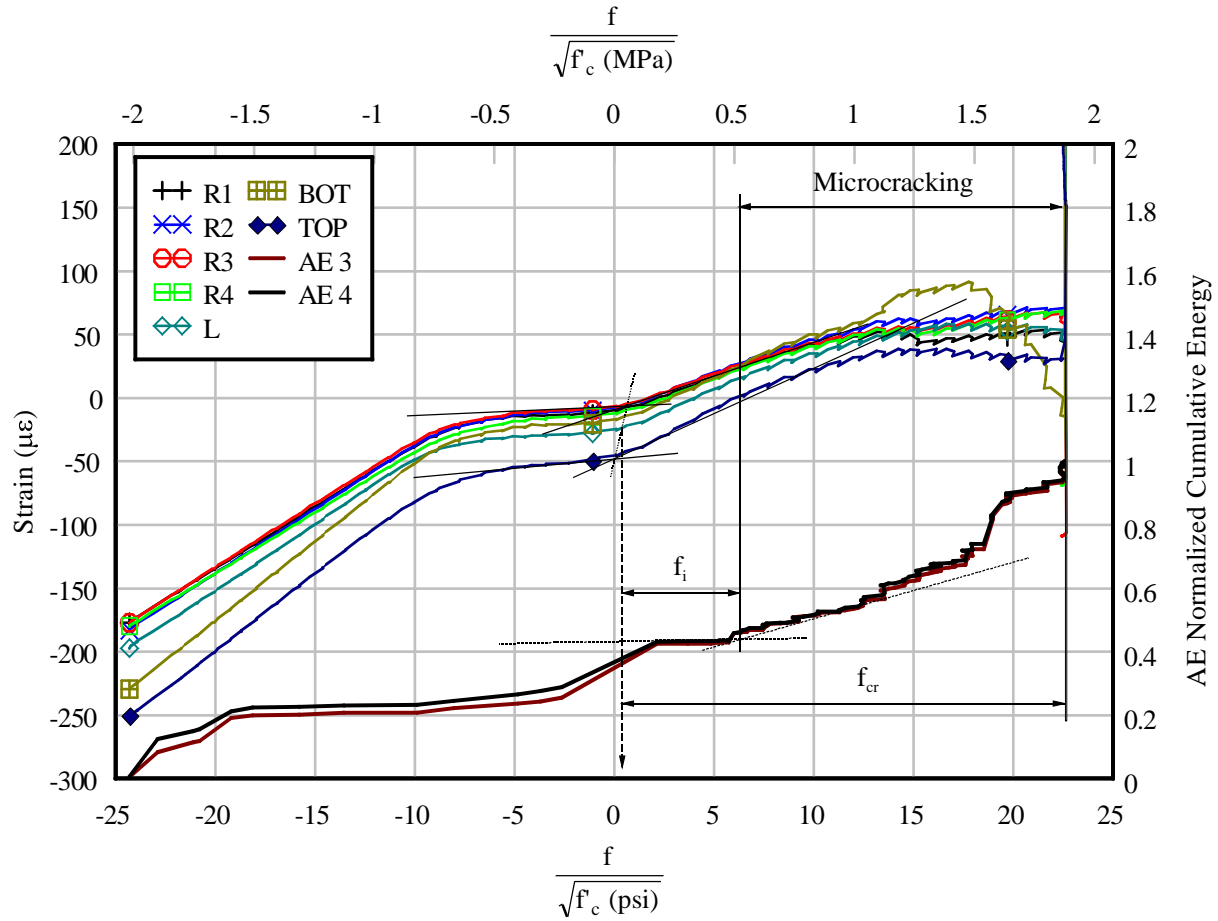


Figure 7-11. Test A non-thermal specimen (stress ratio)

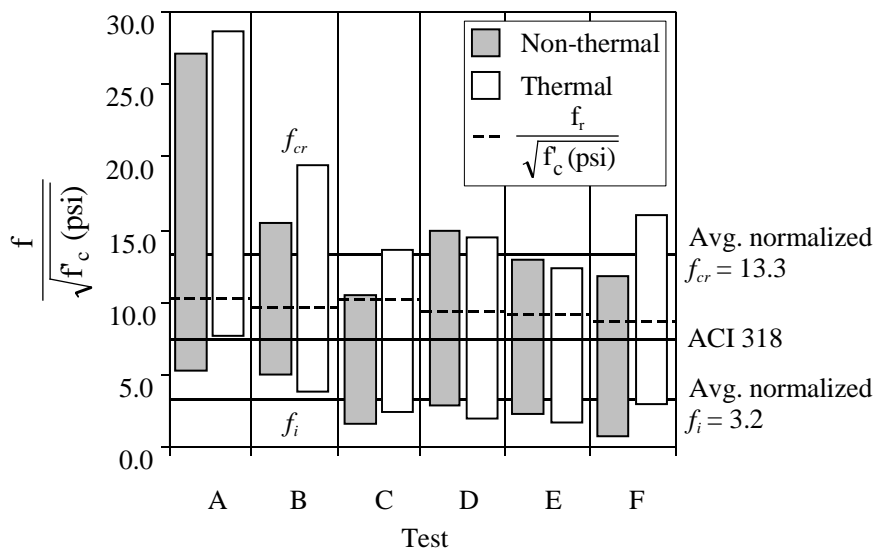


Figure 7-12. Stress ratio ranges of microcracking

## CHAPTER 8 SUMMARY AND CONCLUSIONS

Nonlinear thermal gradients have been measured on concrete bridges in the field and previous research, Phase I of this investigation, confirmed that the self-equilibrating stresses generated by the nonlinear portion of such gradients compare well with those calculated by elastic mechanics principles. According to *AASHTO Guide Specifications for Design and Construction of Segmental Concrete Bridges* (1999), service stresses resulting from thermal gradients must be superimposed on those caused by dead loads, superimposed service loads, creep, and shrinkage. The research presented in this report evaluated the effect that the self-equilibrating stresses generated by the nonlinear thermal gradient have on the cracking behavior of concrete when superimposed on the stresses due to locked-in and applied moments.

Six concrete specimen test sets were loaded to cracking both with and without temperature gradient, to investigate the effects of self-equilibrating tensile stress on cracking behavior. Each test set consisted of two identical prestressed specimens being loaded in direct tension until the concrete cracked. Each specimen had a steel bar through the center to apply a prestress and later a direct tensile force to the concrete. The specimen was constructed with confinement reinforcement around internal anchors on the steel bar at each end. At the center of the specimen, a 2 in. gauge length was left unreinforced. The prestressing bar was debonded at the same location to force cracking to occur in this gauge length. A load frame was instrumented with a load cell and LVDTs. Each specimen was instrumented with strain gauges and acoustic emission sensors. On one prestressed specimen from each test set, a nonlinear negative thermal gradient was imposed on the specimen by an open channel flow of chilled water over

the top surface. This specimen was also instrumented with internal thermocouples to measure the temperature profile across the section.

The procedure for each test included, in sequence, stressing the steel bar in the load frame, casting the concrete specimen, prestressing the concrete specimen after curing, and loading the specimen in direct tension until failure of the concrete. The nonlinear thermal gradient was imposed during application of direct tensile loading for one specimen in each test set to determine the influence of the nonlinear thermal gradient on cracking.

The net tensile stress (or net tensile load) at the initiation of microcracking and the net tensile stress at cracking were determined using measured strain data and cumulative acoustic emission energy. The net tensile stress at the initiation of microcracking and the net tensile stress at visible cracking were compared between specimens within each test set to determine the effect of the self-equilibrating stresses on the cracking behavior. The salient conclusions are as follows:

- With the influence of self-equilibrating tensile stress from a nonlinear negative thermal gradient, an expected decrease in normalized  $f_i$  values for thermal specimens relative to non-thermal specimens should occur. Rather, there was both an observed increase and decrease in normalized  $f_i$  values for thermal specimens relative to non-thermal specimens. This behavior reveals that there may be no significant effect that the nonlinear thermal gradient has on the initiation of cracking behavior.
- Further, the average normalized stress range of microcracking observed in testing was 3.2 to 13.3, with a coefficient of variation of 61% and 31%, respectively. The normalized stress range is similar to that of a typical range of the normalized modulus of rupture of concrete, 5 to 12. These similar ranges further reveal that there may be no significant effect that the nonlinear thermal gradient has on the cracking behavior of concrete. Cracking behavior influenced by any effect of a nonlinear thermal gradient is dominated by the influence of variability associated with concrete in tension.

## CHAPTER 9 RECOMMENDATIONS

In consideration of the discussion and conclusions of this research, the following recommendations have been made:

- The consideration of the nonlinear negative thermal gradient component of the total thermal gradient considered and the structural response to such a gradient as outlined by provisions in the AASHTO LRFD *Bridge Design Specifications* (2007) should be eliminated.
- Further investigation of local thermal gradients and the resulting structural response in segmental box girder flanges and deck should be considered. The local thermal gradient and structural response to that gradient may result in additional stresses that affect the serviceability of the structure.

## APPENDIX A TEST RESULT FIGURES

This appendix includes results of Test A – Test F for the non-thermal and thermal specimens. Each includes strain-load on the primary x-axis and strain-stress on the secondary x-axis.

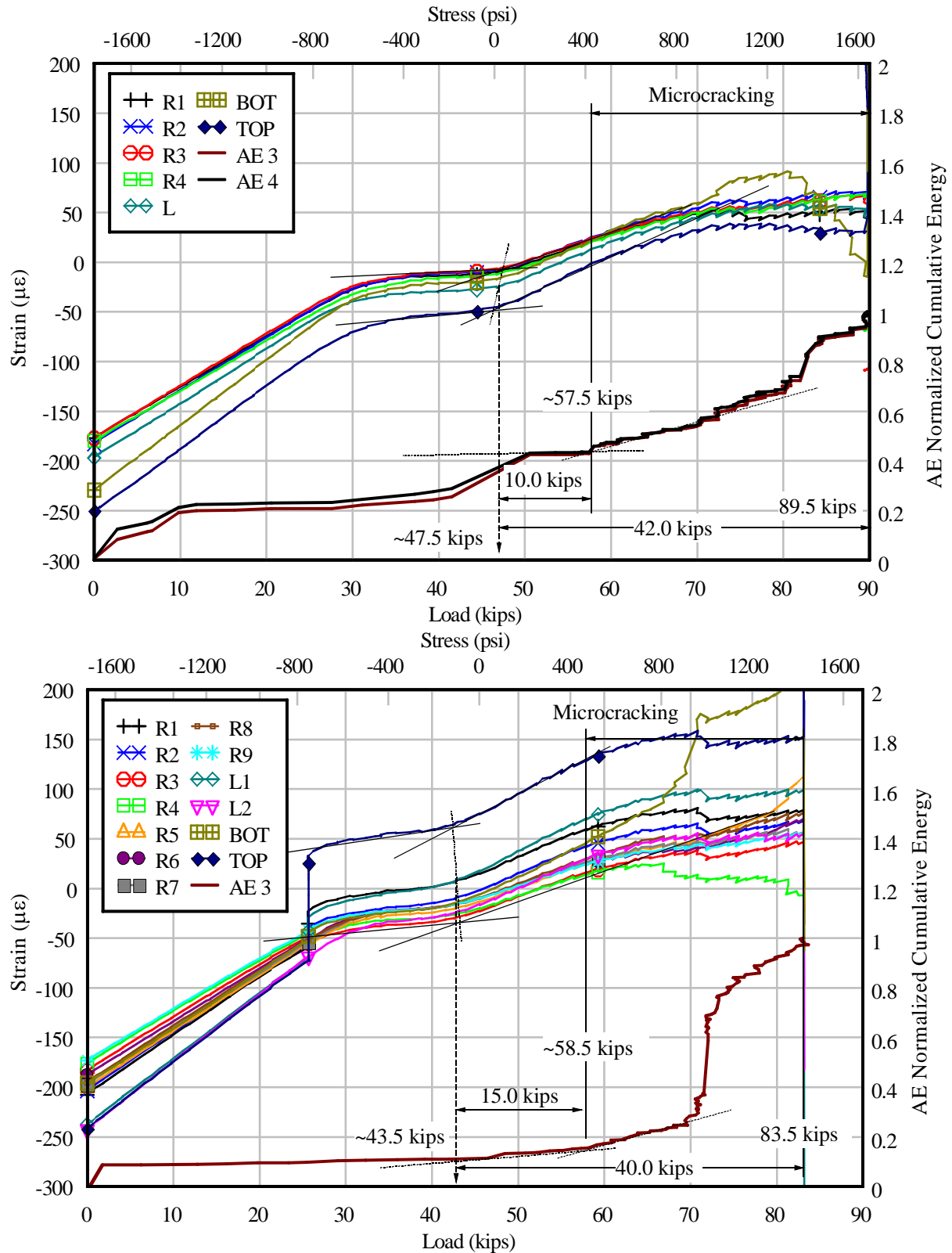


Figure A-1. Test A results for non-thermal specimen (top) and thermal specimen (bottom)

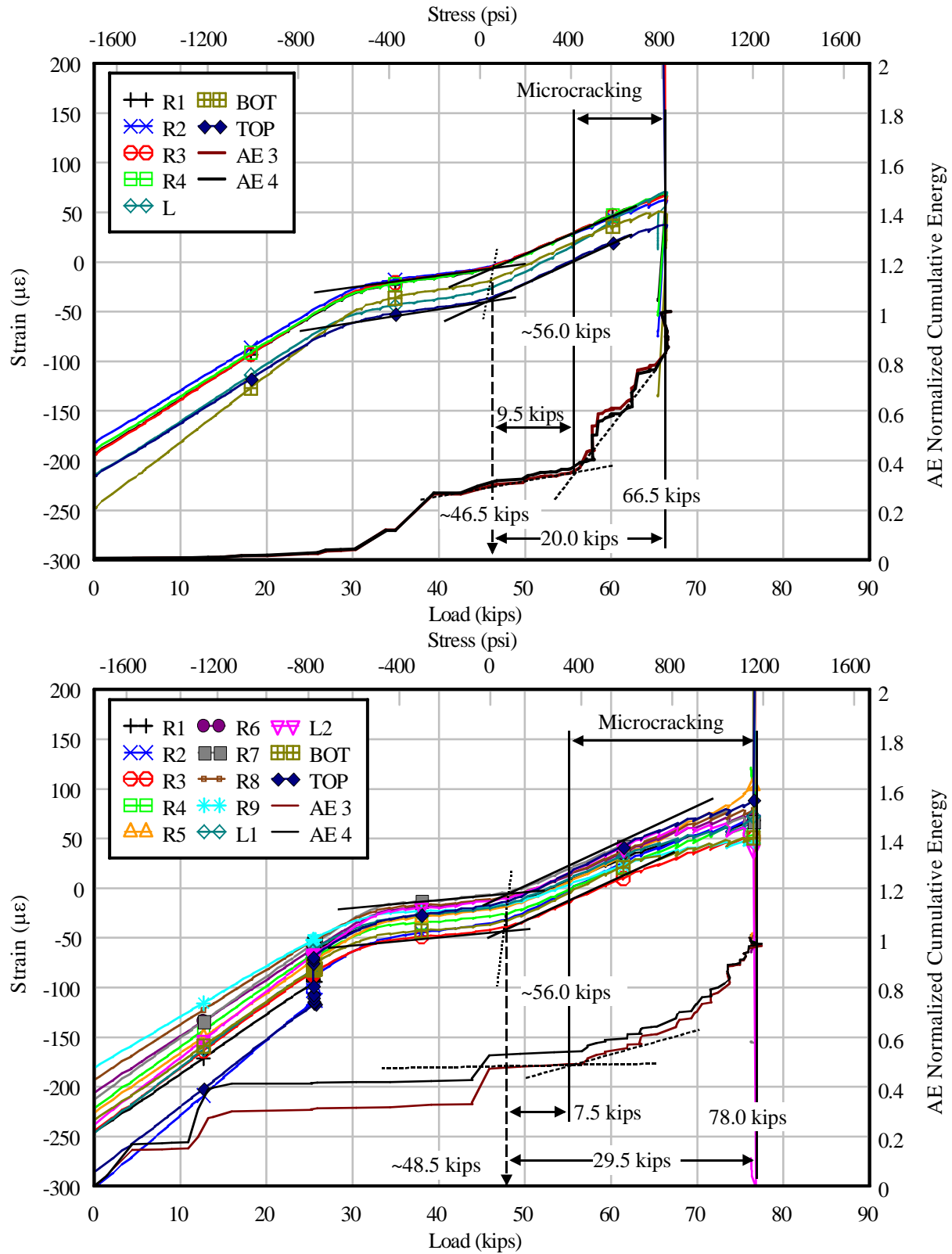


Figure A-2. Test B results for non-thermal specimen (top) and thermal specimen (bottom)

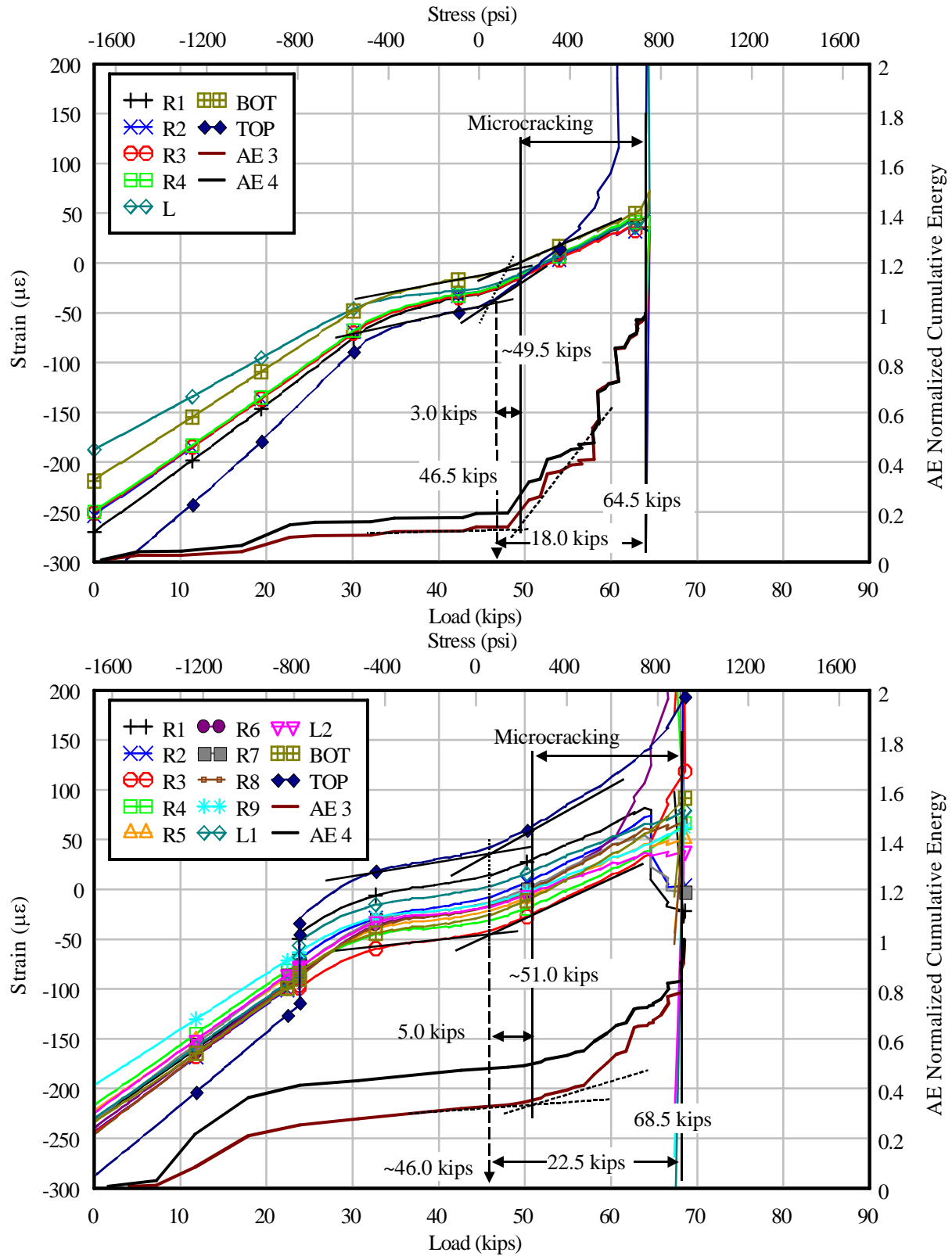


Figure A-3. Test C results for non-thermal specimen (top) and thermal specimen (bottom)

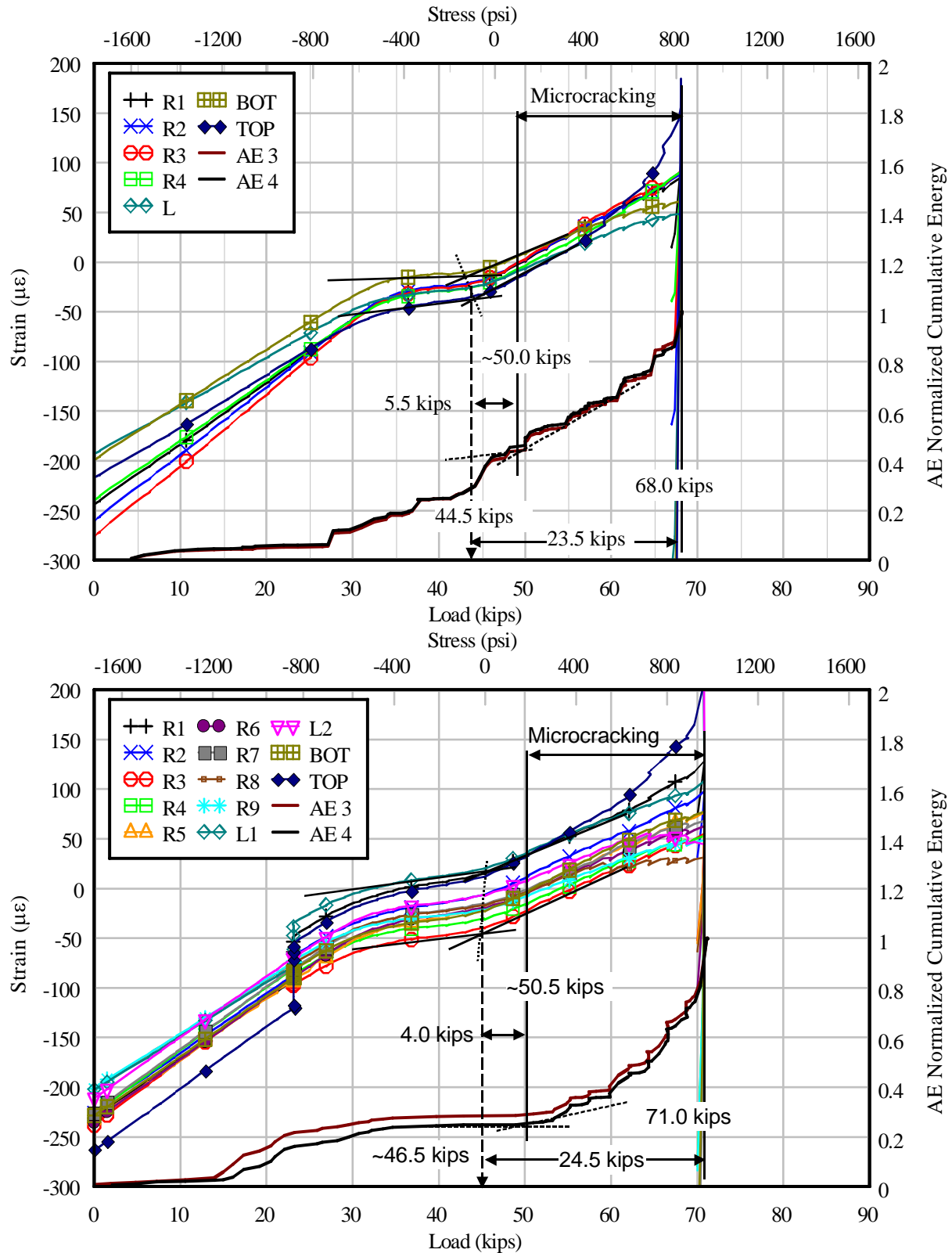


Figure A-4. Test D results for non-thermal specimen (top) and thermal specimen (bottom)

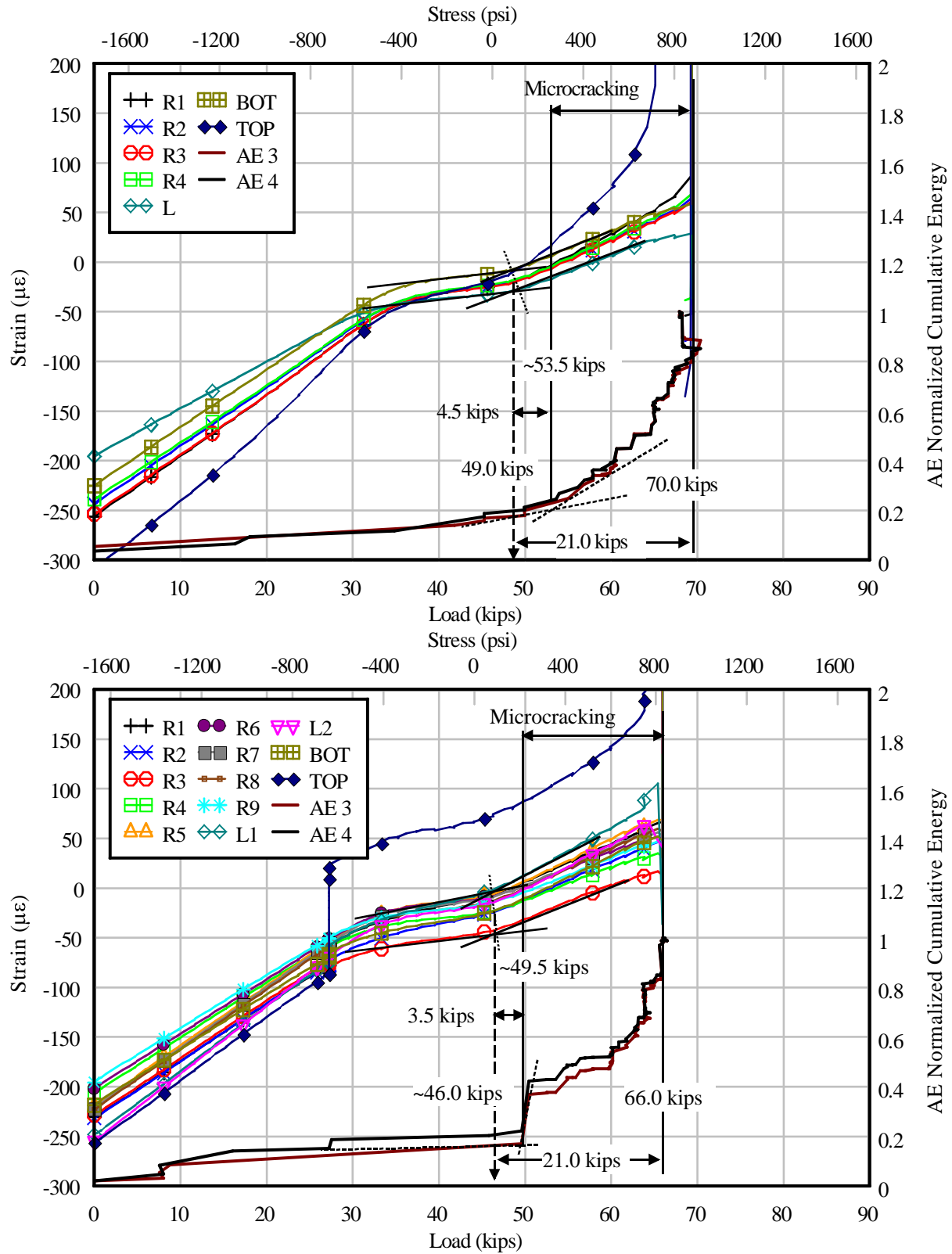


Figure A-5. Test E results for non-thermal specimen (top) and thermal specimen (bottom)

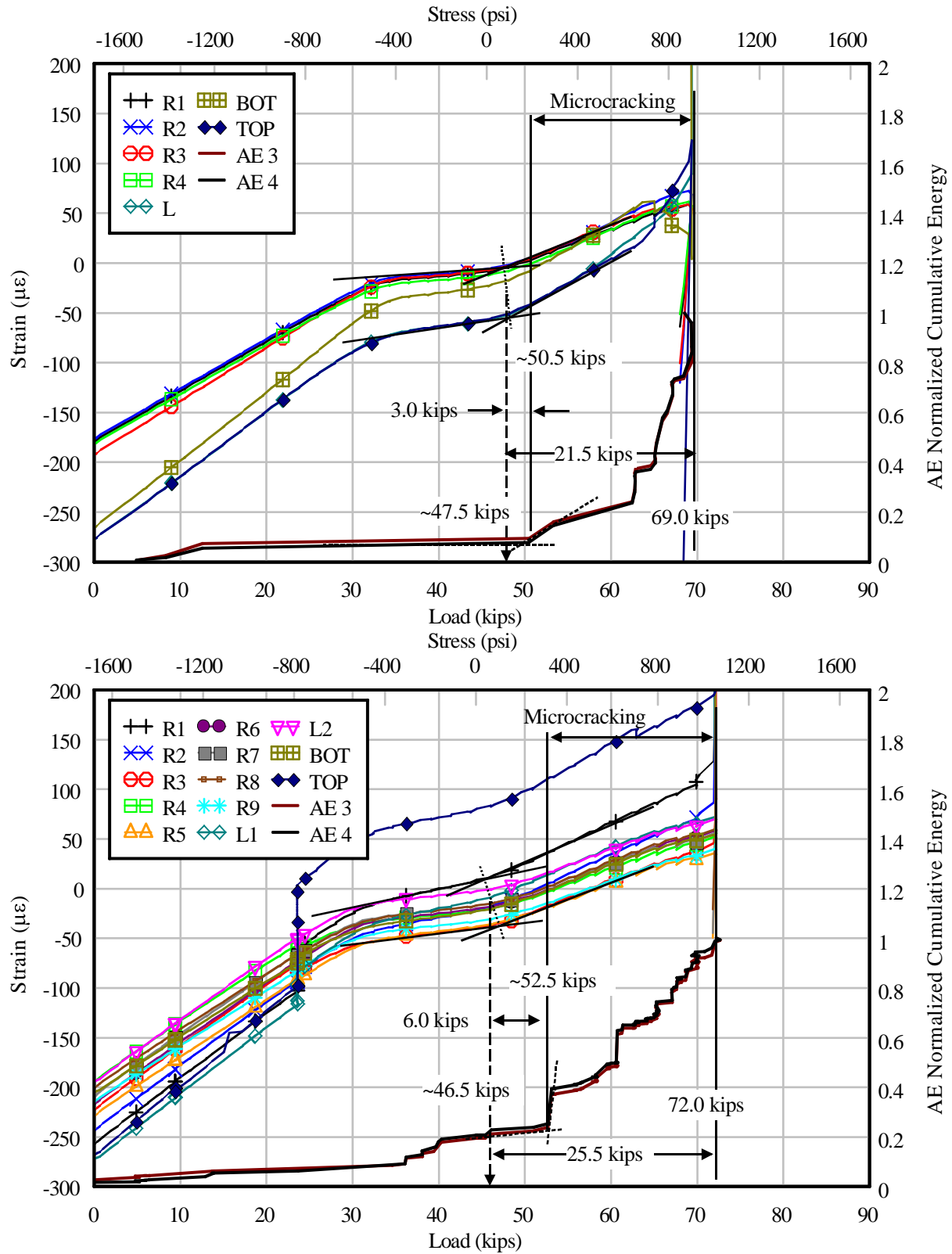


Figure A-6. Test F results for non-thermal specimen (top) and thermal specimen (bottom)

APPENDIX B  
TEST RESULT TABLES

Table B-1. Net tensile load at initial microcracking for non-thermal and thermal tests

	P <sub>i</sub> (kips)		P <sub>i</sub> (kN)		Non-Thermal / Thermal
	Non-Thermal	Thermal	Non-Thermal	Thermal	
Test A	10.0	15.0	44.5	66.7	0.67
Test B	9.5	7.5	42.3	33.4	1.27
Test C	3.0	5.0	13.3	22.2	0.60
Test D	5.5	4.0	24.5	17.8	1.38
Test E	4.5	3.5	20.0	15.6	1.29
Test F	1.5	6.0	6.7	26.7	0.25

Table B-2. Net tensile load at visible cracking for non-thermal and thermal tests

	P <sub>cr</sub> (kips)		P <sub>cr</sub> (kN)		Non-Thermal / Thermal
	Non-Thermal	Thermal	Non-Thermal	Thermal	
Test A	42.0	40.0	186.8	177.9	1.05
Test B	20.0	29.5	89.0	131.2	0.68
Test C	18.0	22.5	80.1	100.1	0.80
Test D	23.5	24.5	104.5	109.0	0.96
Test E	21.0	21.0	93.4	93.4	1.00
Test F	21.5	25.5	95.6	113.4	0.84

Table B-3. Initial stress ratio for non-thermal and thermal tests

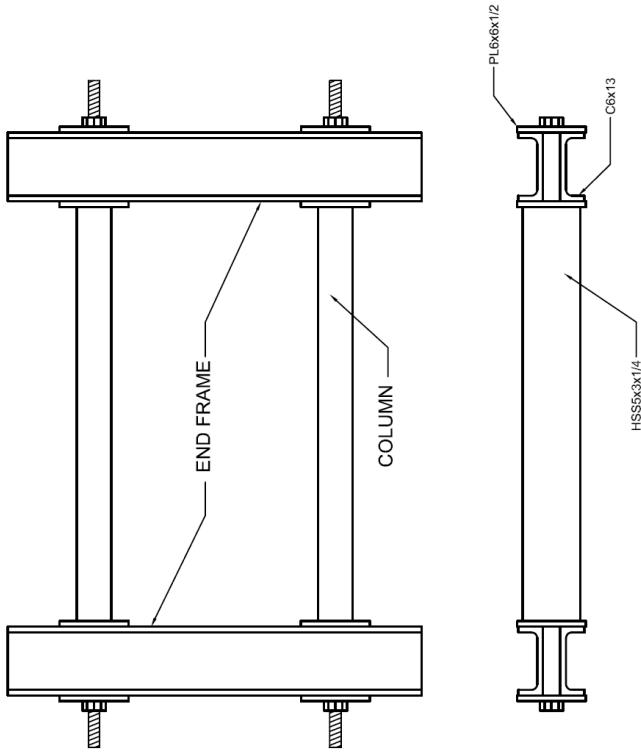
	$\frac{f_i}{\sqrt{f'_c}}$ (psi)		$\frac{f_i}{\sqrt{f'_c}}$ (Mpa)		$\frac{f_r}{\sqrt{f'_c}}$ (psi)	$\frac{f_r}{\sqrt{f'_c}}$ (Mpa)
	Non-Thermal	Thermal	Non-Thermal	Thermal		
Test A	5.2	7.8	0.43	0.65	10.3	0.86
Test B	5.0	3.9	0.42	0.33	9.8	0.81
Test C	1.5	2.5	0.12	0.21	10.1	0.84
Test D	2.8	2.1	0.23	0.17	9.5	0.79
Test E	2.3	1.8	0.19	0.15	9.1	0.76
Test F	0.8	3.1	0.06	0.26	8.8	0.73

Table B-4. Final stress ratio for non-thermal and thermal tests

	$\frac{f_{cr}}{\sqrt{f'_c}} \text{ (psi)}$		$\frac{f_{cr}}{\sqrt{f'_c}} \text{ (Mpa)}$	
	Non-Thermal	Thermal	Non-Thermal	Thermal
Test A	21.9	20.9	1.82	1.73
Test B	10.5	15.5	0.87	1.29
Test C	9.0	11.3	0.75	0.94
Test D	12.1	12.6	1.00	1.04
Test E	10.6	10.6	0.88	0.88
Test F	11.0	13.1	0.92	1.09

APPENDIX C  
LOAD FRAME SHOP DRAWINGS

This appendix includes the shop drawings used in fabrication of the load frame.



**TOTAL ITEM LIST FOR FRAME CONSTRUCTION - (2)**

ITEM #	QUANTITY	ITEM	DIMENSIONS
1	4	C6X13	3'-0"
2	6	C6X13	0'-6"
3	4	HSS 5X3X1/4	3'-0"
4	9	PL 6X6X1/2	6x6x $\frac{1}{2}$ WITH 1 $\frac{3}{8}$ DIA.
5	16	PL 6X6X1/2	6x6x $\frac{1}{2}$ WITH 1 $\frac{1}{8}$ DIA.
6	6	PL 9X6X1/2	9x6x $\frac{1}{2}$ WITH 1 $\frac{3}{8}$ DIA.
7	16	1 $\frac{1}{2}$ X1 BAR	1 $\frac{1}{2}$ X1X6

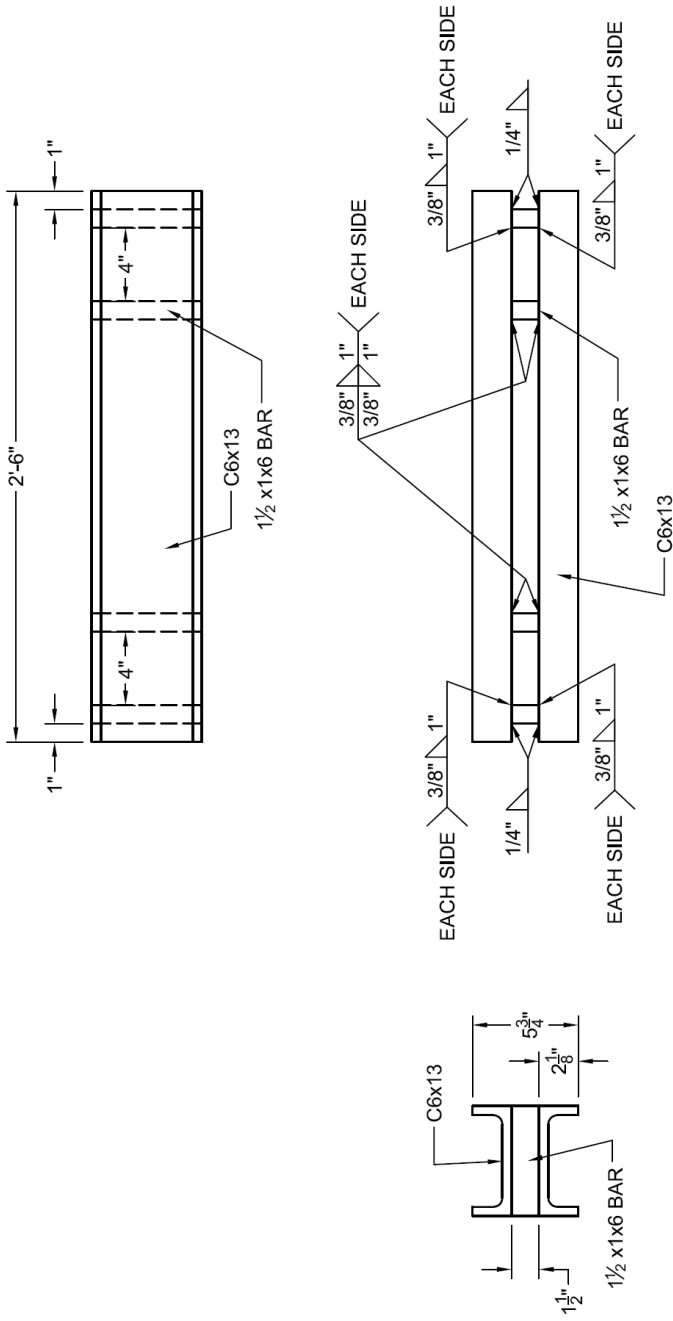
**(2) - FRAME OVERVIEW**

SCALE: NTS

University of Florida  
 Dept. of Civil and Coastal Engineering  
 Designer: Nathan Currier  
 Contact: 352-231-0465  
 Date: 02-27-08

**SHEET: 1 OF 6**

Figure C-1. Frame overview



ITEM LIST FOR END FRAME - (4)

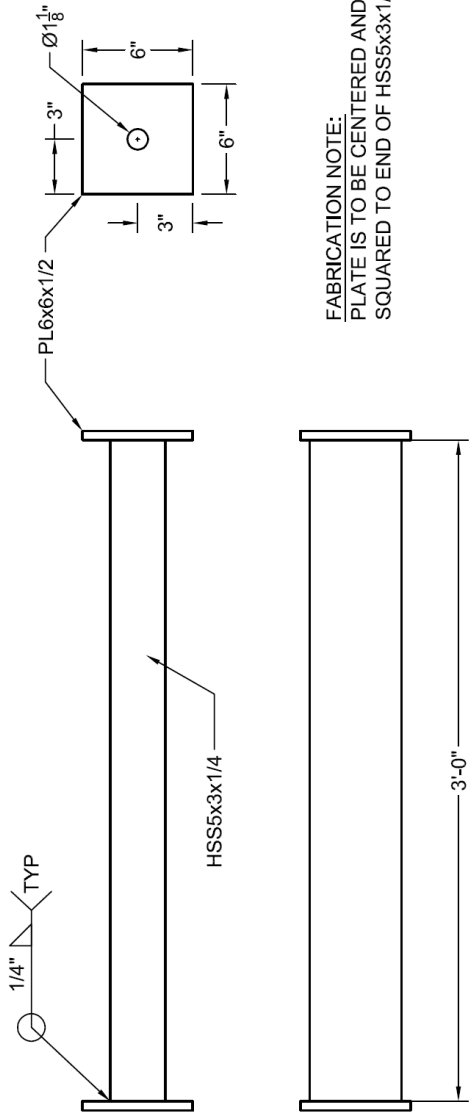
ITEM #	QUANTITY	ITEM	DIMENSIONS
1	8	C6X13	3'-0"
7	16	1/2X1 BAR	1/2X1X6

**(4) - END FRAME**

SCALE: 1 1/2" = 1'-0"

University of Florida  
 Dept. of Civil and Coastal Engineering  
 Designer: Nathan Currier  
 Contact: 352-231-0465  
 Date: 02-27-08

Figure C-2. End frame detail



**ITEM LIST FOR COLUMN - (4)**

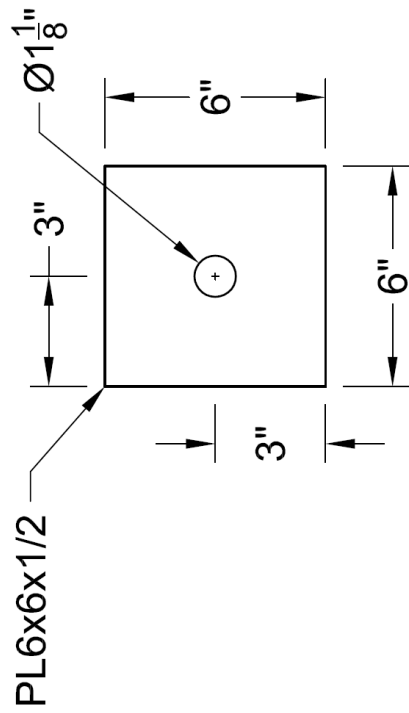
ITEM #	QUANTITY	ITEM	DIMENSIONS
3	4	HSS 5X3X1/4	3'-0"
5	8	PL 6X6X1/2	6x6x1/2 WITH 1 1/8 DIA.

**(4) - COLUMN**  
SCALE: 1 1/2" = 1'-0"

University of Florida  
 Dept. of Civil and Coastal Engineering  
 Designer: Nathan Currier  
 Contact: 352-231-0465  
 Date: 02-27-08

**SHEET: 3 OF 6**

Figure C-3. Column detail



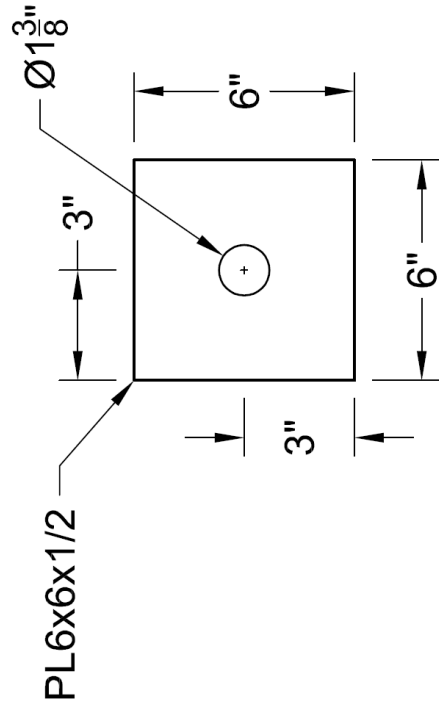
ITEM LIST FOR PLATE WITH 1/8" DIA - (8)		
ITEM #	QUANTITY	DIMENSIONS
5	8	PL 6X6X1/2 6x6x1/2 WITH 1/8" DIA.

**(8) - PLATE WITH 1 1/8" DIA**  
 SCALE: 3" = 1'-0"

University of Florida  
 Dept. of Civil and Coastal Engineering  
 Designer: Nathan Currier  
 Contact: 352-231-0465  
 Date: 02-27-08

**SHEET: 4 OF 6**

Figure C-4. Plate detail 1



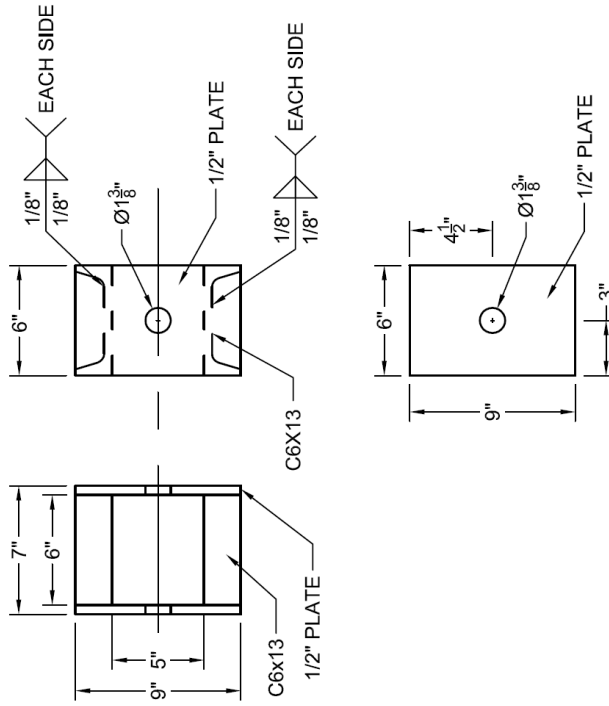
TOTAL ITEM LIST FOR PLATE WITH 1 3/8" DIA - (9)		
ITEM #	QUANTITY	ITEM DIMENSIONS
4	9	PL 6X6X1/2 6x6x1/2 WITH 1 3/8" DIA.

**(9) - PLATE WITH 1 3/8" DIA**  
 SCALE: 3" = 1'-0"

University of Florida  
 Dept. of Civil and Coastal Engineering  
 Designer: Nathan Currier  
 Contact: 352-231-0465  
 Date: 02-27-08

**SHEET: 5 OF 6**

Figure C-5. Plate detail 2



ITEM LIST FOR PRESTRESS CHAIR - (3)		
ITEM #	QUANTITY	ITEM DIMENSIONS
2	6	C6X13 0'-6"
6	6	PL 9X6X1/2 9X6X1/2 WITH 1 3/8 DIA.

### (3) - PRESTRESS CHAIR

SCALE: 1 1/2" = 1'-0"

University of Florida  
 Dept. of Civil and Coastal Engineering  
 Designer: Nathan Currier  
 Contact: 352-231-0465  
 Date: 02-27-08

**SHEET: 6 OF 6**

Figure C-6. Prestress chair detail

## APPENDIX D SPECIMEN DESIGN AND TEST SETUP DRAWINGS

This appendix includes drawings for the fabrication of the test specimen.

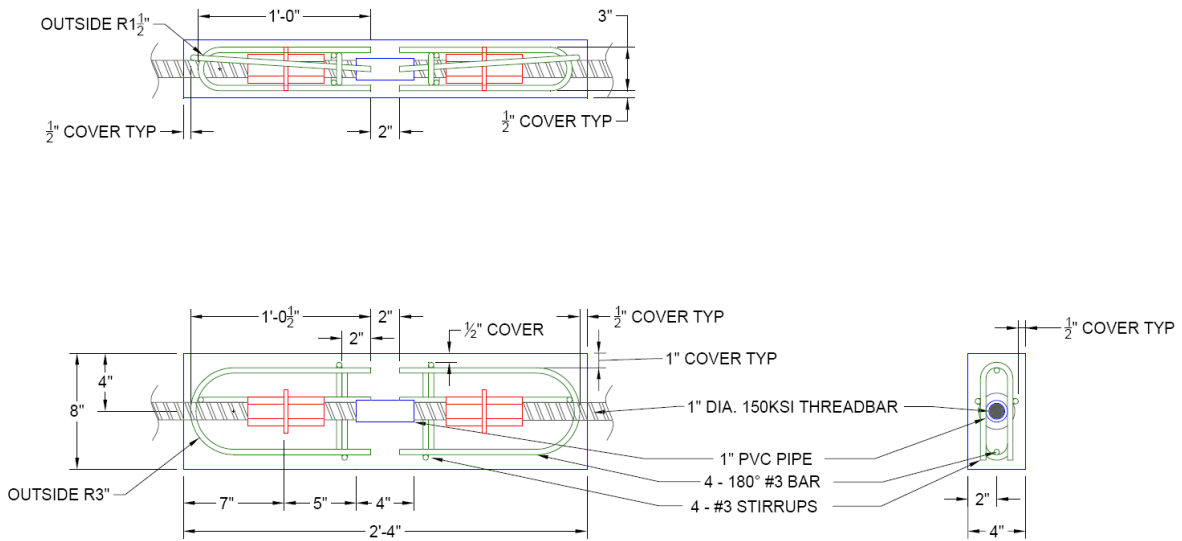


Figure D-1. Specimen fabrication drawings

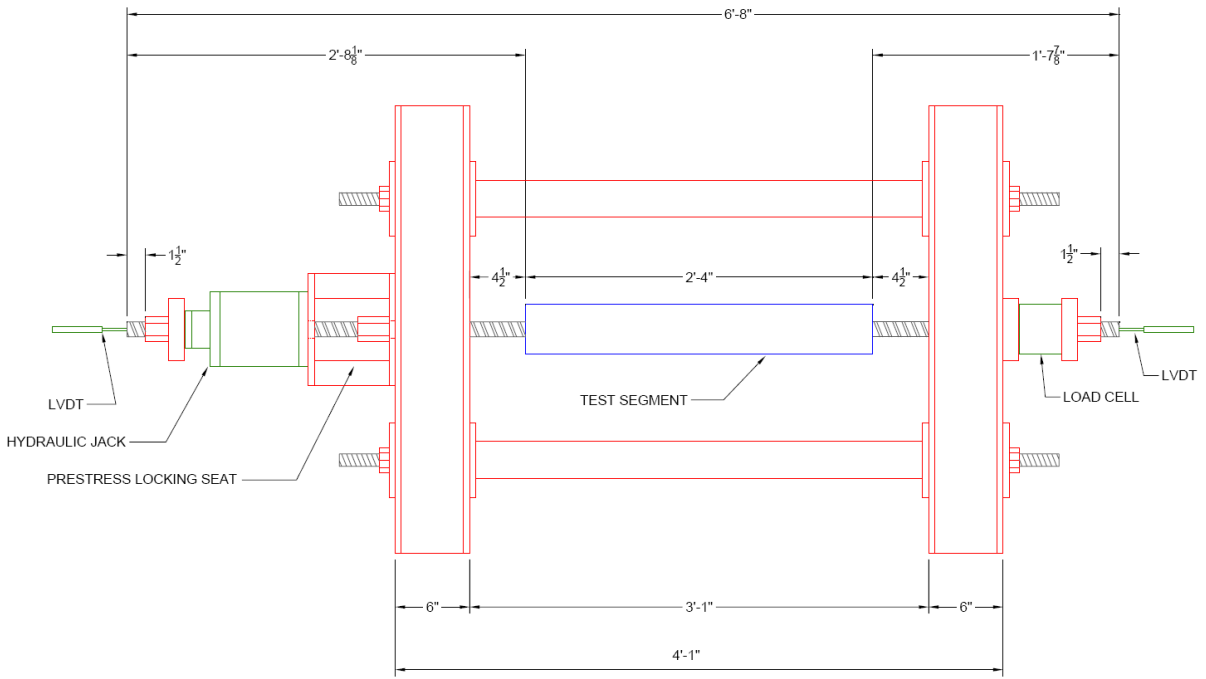


Figure D-2. Test setup detail

## LIST OF REFERENCES

- American Association of State Highway and Transportation Officials (AASHTO), 1989, "AASHTO Guide Specifications, Thermal Effects in Concrete Bridge Superstructures," Washington D.C.
- AASHTO, 1999, "Guide Specifications for Design and Construction of Segmental Concrete Bridges," 2<sup>nd</sup> Ed., Washington, D.C.
- AASHTO, 2007, "AASHTO LRFD Bridge Design Specifications," 4<sup>th</sup> Ed., Washington, D.C.
- American Concrete Institute (ACI) Committee 209, 2008, "Prediction of Creep, Shrinkage, and Temperature Effects in Concrete Structures (ACI 209R-92)," American Concrete Institute, Farmington Hills, Michigan.
- ACI Committee 224, 2004, "Cracking of Concrete Members in Direct Tension (ACI 224.2R-92)," American Concrete Institute, Farmington Hills, Michigan.
- ACI Committee 318, 2005, "Building Code Requirements for Structural Concrete (318-05) and Commentary (318R-05)," American Concrete Institute, Farmington Hills, Michigan.
- ACI Committee 435, 1995, "Control of Deflection in Concrete Structures (ACI 435R-95)," American Concrete Institute, Farmington Hills, Michigan.
- American Society for Testing and Materials (ASTM) C 39-01, 2001, "Standard Test Method for Compressive Strength of Concrete Cylinders Cast in Place in Cylindrical Molds," American Society of Testing and Materials, West Conshohocken, PA.
- ASTM C 78-08, 2008, "Standard Test Method for Flexural Strength of Concrete (Using Simple Beam with Third-Point Loading)," American Society of Testing and Materials, West Conshohocken, PA.
- ASTM C 138-09, 2009, "Standard Test Method for Density (Unit Weight), Yield, and Air Content (Gravimetric) of Concrete," American Society of Testing and Materials, West Conshohocken, PA.
- ASTM C 143-08, 2008, "Standard Test Method for Slump of Hydraulic-Cement Concrete," American Society of Testing and Materials, West Conshohocken, PA.
- ASTM C 496-04, 2004, "Standard Test Method for Splitting Tensile Strength of Cylindrical Concrete Specimens," American Society of Testing and Materials, West Conshohocken, PA.
- ASTM C 566-97, 2004, "Standard Test Method for Total Evaporable Moisture Content of Aggregate by Drying," American Society of Testing and Materials, West Conshohocken, PA.
- ASTM E 1316-06a, 2006, "Standard Terminology for Nondestructive Examinations," ASTM International, West Conshohocken, Pa., 33 pp.

Colombo, S.; Forde, M.C.; Main, I.G.; Halliday, J.; Shigeishi, M., 2005 “AE Energy Analysis on Concrete Bridge Beams,” *Materials and Structures*, V. 38 No. 9, Nov., pp. 851-856.

Kaplan, M.F., 1963, “Strains and Stresses of Concrete at Initiation of Cracking and Near Failure,” *Journal of the American Concrete Institute*, V. 60, No. 7, July. pp. 853-860.

Labuz, J. F.; Cattaneo, S.; Chen, L., 2001, “Acoustic Emission at Failure in Quasi-Brittle Materials,” *Construction and Building Materials*, V. 15, No. 5-6, July-Sept., pp. 225-233.

Mahama, F.; Consolazio, G.R.; Hamilton, H.R.; 2007, “Validation of Stresses Caused by Thermal Gradients in Segmental Concrete Bridges,” Doctoral Dissertation, University of Florida, Gainesville, FL.

Neville, A. M., 1995, *Properties of Concrete*, 4<sup>th</sup> Ed., Pearson Education Limited, London, England. pp. 289-600.

Nielsen, John and Griffin, D.F., 1977, “Acoustic Emission of Plain Concrete,” *Journal of Testing and Evaluation*, JTEVA, Vol. 5, No. 6, pp. 476-483.

Oh, B.H.; Kim, K.S.; Kim, E.J., 2000, “Identification of Damages of Concrete Structures Using Acoustic Emission,” *American Concrete Institute Journal*, Volume 193, pp. 195-210.

O’Neill, C.; Hamilton, H.R., 2009, “Determination of Service Stresses in Pretensioned Beams,” FDOT Contract No. BD 545-78.

Popovics, S., 1998, *Strength and Related Properties of Concrete: A Quantitative Approach*, John Wiley & Sons, New York, NY. pp. 103-157.

Puri, S.; Weiss, J., 2006, “Assessment of Localized Damage in Concrete under Compression Using Acoustic Emission,” *ASCE Journal of Materials in Civil Engineering*, V. 18, No. 3, May-June, pp. 325-333.

Shield, C. K.; Hearn, S. W., 1997, “Acoustic Emission Monitoring as a Nondestructive Testing Technique in Reinforced Concrete,” *ACI Materials Journal*, V. 94, No. 6, Nov.- Dec., pp. 510-519.

Zhen-hai, G., Xiu-qin, Z., 1987, “Investigation of Complete Stress-Deformation Curves for Concrete in Tension,” *ACI Materials Journal*, V. 84, No. 4, July-Aug., pp. 278-285.

## BIOGRAPHICAL SKETCH

The author began his undergraduate education in 2002 at the University of Florida in Gainesville, FL. After graduating with a Bachelor of Science degree in civil engineering in May 2007, the author continued his studies at the University of Florida pursuing a Master of Engineering in civil engineering, with a concentration in structural engineering. The author obtained his degree in December 2009. Upon graduating, he will be pursuing a career in structural engineering at a design firm in Tallahassee, FL.